COLLEGE OF ENGINEERING
Department of Nuclear Engineering

FINAL REPORT

for project entitled

CPM Modeling

Subcontract 4000178743 – Solicitation 6400016556

between

UT-Battelle LLC/Oak Ridge National Laboratory

and

Texas A&M Engineering Experiments Station/Texas A&M University

Principal Investigator: Shaheen Dewji, Ph.D.
Address: TAMU 3133, College Station, TX 77843-3133
Tel: 979-458-8165
E-mail: sdewji@tamu.edu
Date: December 18, 2020

TABLE OF CONTENTS

LIST OF FIGURES iv
LIST OF TABLES v
ACRONYMS AND ABBREVIATIONS vi
EXECUTIVE SUMMARY 7
1. PROJECT OBJECTIVES 8
2. BACKGROUND 9
2.1. Monte Carlo N-Particle (MCNP) Radiation Transport Code 9
2.2. Shift: A Massively Parallel MC Radiation Transport Code 10
2.2.1. Denovo Deterministic Solver Overview 10
2.2.2. CADIS Hybrid Method Overview 12
3. METHODOLOGY 14
3.1. Overview 14
3.2. Project Task Descriptions and Completion Status 16
3.2.1. Task Descriptions 16
3.2.2. Completion Status 19
3.3. MCNP/Shift Detector Response Methodology 20
3.3.1. Response Function Overview 20
3.3.2. MCNP/Shift Response Function Implementation 20
3.3.3. Weight Window Automation Method 22
3.4. Radionuclide CPM Simulation Methodology 23
3.5. Normalization of Final Results for Use in CPM Calculator 23
3.5.1. CPM Area Calculator Activity to CPM Conversion Factor 23
3.5.2. CPM Volume Calculator Activity to CPM Conversion Factor 24
4. BENCHMARK RESULTS 24
4.1. Materials Data 24
4.2. Emission Definition 25
4.3. Preliminary F4 Benchmarks for Exterior Coupling Surface 25
5. RESULTS AND DISCUSSION 29
5.1. Monoenergetic Surface Contamination 29
5.2. Monoenergetic Volumetric Contamination 34
5.3. Radionuclide Interpolation 37
6. CONCLUSIONS AND FUTURE WORK 38

7. ACKNOWLEDGMENTS 39
8. REFERENCES 39
APPENDIX A. Supplemental Data 41
APPENDIX B. Supplemental Figures 52
APPENDIX C. List of Electronically Tabulated Data..... 55

LIST OF FIGURES

Figure 1. The random history of a neutron incident on a slab of material that can undergo fission. 9

Figure 2. Decomposition of 3-D mesh for KBA. In this example, the grid is decomposed on nine processors. 12

Figure 3. A flow chart that summarizes the project methodology. 15

Figure 4. Ludlum Model 44-62 0.5x1 NaI(Tl) schematic line diagram (Ludlum Measurements Inc., 2020). 17

Figure 5. Ludlum Model 44-2 1x1 NaI(Tl) schematic line diagram (Ludlum Measurements Inc., 2020). 17

Figure 6. Canberra/Mirion Model 802-2 NAIS 2x2 Na(Tl) schematic line diagram (Mirion Technologies, 2020). 18

Figure 7. Ludlum Model 44-20 3x3 NaI(Tl) schematic line diagram (Ludlum Measurements Inc., 2020). 18

Figure 8. A full model 2x2-inch NaI(Tl) detector and corresponding void detector shown from left to right, respectively. 21

Figure 9. F4 comparison over the 50 keV spectrum. 26

Figure 10. F4 comparison over the 100 keV spectrum. 27

Figure 11. F4 comparison over the 500 keV spectrum. 27

Figure 12. F4 comparison over the 1 MeV spectrum. 28

Figure 13. F4 comparison over the 3 MeV spectrum. 28

Figure 14. Soil surface contamination 3x3-inch detector response as a function of energy for all requested source-detector distances. 30

Figure 15. Soil surface contamination 2x2-inch detector response as a function of energy for all requested source-detector distances. 31

Figure 16. Surface contamination 3x3-inch detector response as a function of energy for all requested media (source-detector distance of 2.54 cm). 32

Figure 17. Surface contamination 2x2-inch detector response as a function of energy for all requested media (source-detector distance of 2.54 cm). 33

Appendices

Figure B.1. MCNPX Visual Editor rendering of a 2x2-inch detector response problem geometry. 52

Figure B.2. MCNPX Visual Editor rendering of a 2x2-inch void detector response problem geometry. 53

Figure B.3. Total mass attenuation coefficient and energy absorption mass coefficient as a function of photon energy in air (Berger et al,. 2010). 54

LIST OF TABLES

Table 1. Contaminated source depths evaluated (per SOW). 8

Table 2. Discrete energies evaluated (per SOW). 8

Table 3. Breakdown of simulation runs required to obtain CPM detector response data (per initial SOW). 14

Table 4. Results of the preliminary F4 convergence tests. 26

Table 5. Sample MCNP/Shift volumetric contamination full model comparisons. 37

Table 6. Sample soil 3x3-inch detector response results for radionuclides of high concern in emergency response/dose assessment as a function of depth (source-detector distance of 2.54 cm). 37

Table 7. Sample soil 2x2-inch detector response results for radionuclides of high concern in emergency response/dose assessment as a function of depth (source-detector distance of 2.54 cm). 38

Appendices

Table A.1. Definition of material composition for radiation transport simulations. 41

Table A.2. Densities and mass attenuation coefficients and infinite thickness depths for six media for gamma-emitting radionuclide emission energies. 42

Table A.3. Densities and mass attenuation coefficients and infinite thickness depths for six media for discrete gamma-ray emission energies. 46

Table A.4. Densities and mass attenuation coefficients and infinite (4) mean free path depths for discrete gamma-ray emission energies to define contamination plane radius. 51

ACRONYMS AND ABBREVIATIONS

Bq	becquerel
CADIS	Consistent Adjoint Driven Importance Sampling
Ci	curie
CPM	Counts per Minute
EPA	Environmental Protection Agency
I/O	input/output
ICRP	International Commission on Radiological Protection
KBA	Koch-Baker-Alcouffe
MC	Monte Carlo
MCNP	Monte Carlo N-Particle Transport
NaI(Tl)	sodium iodide (thallium-doped)
ORNL	Oak Ridge National Laboratory
RNSD	Reactor and Nuclear Systems Division
SOW	Statement of Work
sp	source particle
TAMU	Texas A&M University

EXECUTIVE SUMMARY

The Health Risk and Regulatory Analysis team at Oak Ridge National Laboratory (ORNL) has requested modeling research for validation of the Environmental Protection Agency's (EPA) Counts-Per-Minute (CPM) calculator. Radiation transport modeling using the Monte Carlo N-Particle (MCNP) radiation transport code, and hybrid Monte Carlo code, Shift, were employed to model detector responses four NaI(Tl) scintillation detectors (0.5x1, 1x1, 2x2, and 3x3-inch) for various depths of gamma-ray contamination distributed in various media. Source-detector distances of 0.5 cm, 1 cm, 2.54 cm, 10 cm, and 30 cm were modeled. Media of soil, concrete, wood, steel, drywall, glass, and drywall were evaluated for contamination depths ranging from surface to a depth of an infinite thickness in each medium for photon energies ranging from 20 keV to 3 MeV. Monoenergetic response function data for each of the media, contamination depths, and detectors were calculated using MCNP for the Surface CPM energy deposition. Shift was harnessed to increase computational speed of particle transport in high attenuating media for Volume CPM to obtain cell fluxes. Volume cell flux values from Shift were integrated with a response function from MCNP to convert cell flux to energy deposition. All simulations were limited to primary gamma-ray emissions from radionuclides. Bremsstrahlung from beta-emitting radionuclides was not modeled in the scope of this work, but is recommended to accurately model the NaI(Tl) detector response to photons emitted from contaminated media. Interpolation of the monoenergetic to expected radionuclide emissions > 20 keV were conducted using the International Commission on Radiological Protection (ICRP) Publication 107 decay data. Prioritized simulations for the 2x2 and 3x3 detector have been highlighted in this report. All data tabulated have been provided in an electronic accompaniment to this report. It must be noted that the response functions generated here do not replace required experimental validation of detector responses, as computational simulation tools do not permit the real simulation of detector response due to dead time, gain shift, and pulse-pile up effects.

1. PROJECT OBJECTIVES

The Health Risk and Regulatory Analysis team at Oak Ridge National Laboratory (ORNL) has requested modeling research for validation of the Environmental Protection Agency's (EPA) Counts-Per-Minute (CPM) calculator. The CPM Calculator predicts radiation detector readings in counts per minute that correspond to radioactivity (measured in pCi) contaminant concentration levels permitting site remediation, or for any level of interest. The CPM Calculator provides conversions for the following: surveying surface contamination and volumetric contamination. The task description given below outlines the work conducted by Texas A&M University (TAMU) per the Statement of Work (SOW) from ORNL.

In collaboration with ORNL, TAMU has developed parametric bounds for modeling using the radiation transport codes Monte Carlo N-Particle (MCNP) (Werner et al., 2017) and Shift (Pandya et al., 2016) for CPM Calculator validation. The MCNP v6.2 radiation transport code was utilized for validation modeling of the CPM surface calculator (Werner et al., 2017). Preliminary analyses identified Shift as the preferred radiation transport code for validation modeling of the CPM volume calculator. Parameters modeled included the following: Contaminated media radii, photon energies, discrete Superfund radionuclides of interest (^{241}Am, ^{60}Co, ^{137m}Ba/^{137}Cs, ^{3}H, ^{129}I, ^{131}I, ^{238}Pu, ^{239}Pu, ^{240}Pu, ^{226}Ra, ^{228}Ra, ^{220}Rn, ^{222}Rn, ^{90}Sr, ^{99}Tc, ^{228}Th, ^{230}Th, ^{232}Th, ^{234}U, ^{235}U, ^{238}U/^{234m}Pa), NaI(Tl) scintillation detector configurations, source-detector distances, and source material compositions. Upon development and approval of MCNP and Shift model input files created by TAMU by ORNL, TAMU executed MCNP and Shift modeling for the NaI(Tl) scintillation detectors currently available in the CPM Calculator (0.5x1, 1x1, 2x2, and 3x3-inch). Source-detector distances of 0.5 cm, 1 cm, 2.54 cm, 10 cm, and 30 cm were modeled. Media of soil, concrete, wood, steel, glass, and drywall were evaluated for contamination depths identified in Table 1. Table 2 identifies the 19 discrete photon energies that were evaluated. These energies fall between 20 keV and 3 MeV, which correspond to the energies current detectors can discern.

Table 1. Contaminated source depths evaluated (per SOW).

Material	Ground plane	1 cm	2 cm	3 cm	5 cm	15 cm	infinite
Soil	Yes	Yes	Yes	Yes	Yes	Yes	Yes
Concrete	Yes	Yes	Yes	Yes	Yes	Yes	Yes
Wood	Yes	Yes	Yes	Yes	Yes	No	No
Steel	Yes	Yes	Yes	Yes	Yes	Yes	No
Glass	Yes	Yes	Yes	Yes	No	No	No
Drywall	Yes	Yes	Yes	Yes	No	No	No

Table 2. Discrete energies evaluated (per SOW).

1.	0.02 MeV	8.	0.1 MeV	14.	0.6 MeV
2.	0.03 MeV	9.	0.15 MeV	15.	0.8 MeV
3.	0.04 MeV	10.	0.2 MeV	16.	1.0 MeV
4.	0.05 MeV	11.	0.3 MeV	17.	1.5 MeV
5.	0.06 MeV	12.	0.4 MeV	18.	2.0 MeV
6.	0.07 MeV	13.	0.5 MeV	19.	3.0 MeV
7.	0.08 MeV				

2. BACKGROUND

2.1. Monte Carlo N-Particle (MCNP) Radiation Transport Code

MCNP is a stochastic method that is widely used to solve radiation transport problems in reactor physics, shielding, dosimetry, radiation detection and measurements, and various other applications of interest. The Monte Carlo (MC) method enables detailed, explicit geometric, energy, and angular representations and hence is considered the most accurate method available for solving complex radiation transport problems (Wagner et al., 2011). MCNP functions by simulating the individual average particle behavior in a given environment based on sampling of the probability density of particles in phase space. The "behavior" of a particle may be described by the types of interactions (neutron capture, photon scatter, photon leakage, etc.) or "events" that are sampled from probability distributions containing transport data based on the selection of a pseudorandom number. In MCNP, the lifetime of an individual particle from birth until termination (due to absorption, escape from the problem boundary) is described as its random "history." An example of a particle's random history may be visually depicted by Figure 1.

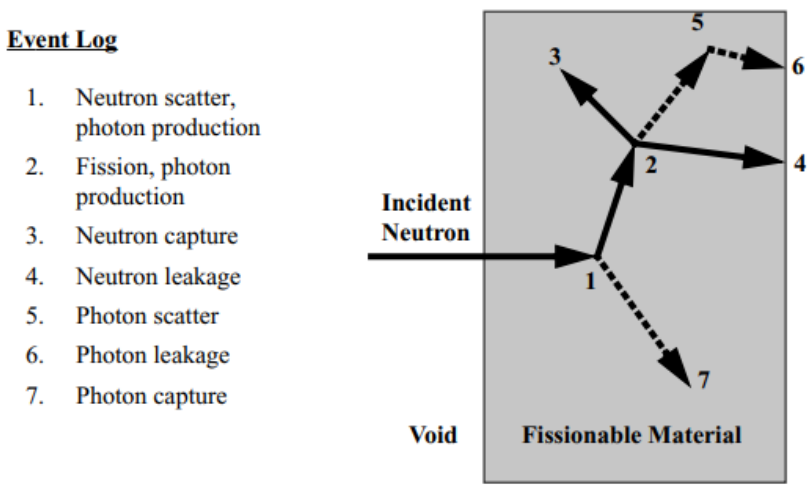

Figure 1. The random history of a neutron incident on a slab of material that can undergo fission.
Numbers between 0 and 1 are selected randomly to determine what (if any) and where interaction takes place, based on the rules (physics) and probabilities (transport data) governing the processes and materials involved (X-5 Monte Carlo Team, 2003).

At the end of the simulation, the final average quantities of interest known as tallies (such as flux, detector pulse, dose, etc.) are estimated from the distribution of all histories and have an associated uncertainty (relative error) that is proportional to one over the square root of the total number of histories for statistically well-behaved simulations. Therefore, the uncertainty may be decreased by increasing the number of histories simulated in the problem to coincide with the "law of large numbers," where the sample mean approaches the population mean as the sample size increases. While MCNP is considered to be the most accurate method available for solving complex radiation transport problems, it possesses the inherent disadvantage of being computationally expensive as the required number of histories to reach proper convergence (less than 5% for detector pulse height) is increased for complex problems (X-5 Monte Carlo Team, 2003).

2.2. Shift: A Massively Parallel MC Radiation Transport Code

Shift is a massively parallel (scalable from laptops to supercomputers) MC radiation transport package that implements hybrid methods (deterministic coupled with stochastic) to obtain a more computationally efficient solution to problems of interest, as opposed to purely stochastic MC. Shift is capable of supporting model definitions (i.e. material compositions, spatial geometries, sources, and tallies) from several formats; MCNP5 model definitions are currently supported (Pandya et al., 2016). Traditional deterministic methods commonly function by implementing the discrete ordinates (S_n) method, where average particle behavior is described by approximating the steady-state integro-differential Boltzmann transport equation through source iteration. The discrete ordinates method visualizes the phase space to be divided into many small boxes, and the particles move from one box to another (X-5 Monte Carlo Team, 2003). In contrast, the integral transport equation is indirectly solved in the stochastic MC method (MCNP) through probability distribution sampling methods.

2.2.1. Denovo Deterministic Solver Overview

A 3-D discrete ordinates transport solver utilized in Shift, known as Denovo, discretizes (conversion of continuous space to equivalent discrete space) the steady-state Boltzmann transport equation in space, angle, and energy to approximate the adjoint fluxes (importance functions that describe the expected tally contribution of particles) that are used to generate variance reduction parameters for accelerating fixed-source MC simulations (Wagner et al., 2011). The CPM Calculator photon sources are fixed, following the matrix equation, i.e.

$$Ax = b \qquad [1]$$

as opposed to a k-eigenvalue sources, following the characteristic equation, i.e.

$$FAx = \left(\frac{1}{k}\right) x\,. \qquad [2]$$

For brevity, all equations shown to demonstrate Shift's capabilities are derived. The steady-state Boltzmann transport equation solved in Denovo is given by (Evans et al., 2010):

$$\hat{\Omega} \cdot \nabla\psi(r,\Omega,E) + \sigma(r,E)\psi(r,\Omega,E) = \int_0^\infty \int_{4\pi} \sigma_s(r,\Omega' \to \Omega, E' \to E) \times \psi(r,\Omega',E')d\Omega' dE' + q_{e(r,\Omega,E)}\,. \qquad [3]$$

Here, the state is defined by the angular flux ψ, and the independent variables are r = (x,y,z) (in centimeters); $\Omega = (\theta, \varphi)$ (in steradians); and E (in mega-electron-volts) representing space, angle, and energy, respectively (Evans et al., 2010). This equation may be used to describe how various particle types (i.e. neutrons, photons) travel through a medium. The left-hand side terms of Eq. 3 describe the net transport (leakage) and total interactions that the particle undergoes, respectively. The right-hand side of Eq. 3 describes the total accumulated source density. Eq. 3 is converted to

a discrete angular form that accounts for anisotropic scattering of the source within a problem geometry as shown (Evans et al., 2010):

$$\hat{\Omega}_a \cdot \nabla \psi_a^g(r) + \sigma^g(r)\psi_a^g(r) = \sum_{g'=0}^{G}\sum_{l=0}^{N} \sigma_{sl}^{gg'}(r) \times \left[Y_{10}^e(\Omega_a)\phi_{10}^{g'}(r) + \sum_{m=1}^{l}\left(Y_{lm}^e(\Omega_a)\phi_{lm}^{g'}(r) + Y_{lm}^0(\Omega_a)\vartheta_{lm}^{g'}(r)\right)\right] + q_e^g(r,\Omega_a)\,. \quad [4]$$

In simple terms, Eq. 4 represents the continuous steady-state Boltzmann transport equation in a discrete space, such that Denovo can solve for the flux component through discretization over the problem geometry "mesh" that is defined by the user with respect to space and angle. The left- and right-hand sides of Eq. 4 follow the same principle described by Eq. 3, where left-hand side describes the net transport (leakage) and total interactions that the particle undergoes, and the right-hand side describes the total accumulated source density. Eq. 4 accounts for group (g) scattering (with respect to energy and angle), as well as even and odd spherical harmonics functions (Y^e, Y^o) used to evaluate Legendre polynomials that expand the angular flux scattering cross section.

Eq. 4 may be expressed in operator form (Evans et al., 2010):

$$L\psi = MS\phi + q_e = Q\,. \quad [5]$$

The same principle applies, where "L" represents the differential transport operator describing the net transport and total interactions of the source (left-hand side of Eq. 3 and 4). The "M" operator is used to convert the harmonic moments to discrete angles; the "S" operator defines the group transfer cross sections for particles (scattering from one energy group to another), and q_e represents the external source term (for photons this is negligible in the current study). Eq. 6 may be further expanded to depict what Denovo is solving in matrix form (Evans et al., 2010):

$$\boldsymbol{L}\begin{pmatrix}[\psi]_0\\ [\psi]_1\\ \vdots\\ [\psi]_G\end{pmatrix} = \boldsymbol{M}\begin{pmatrix}[\mathrm{S}]_{00} & [\mathrm{S}]_{01} & \cdots & [\mathrm{S}]_{0\mathrm{G}}\\ [\mathrm{S}]_{10} & [\mathrm{S}]_{11} & \cdots & [\mathrm{S}]_{1\mathrm{G}}\\ \vdots & \vdots & \ddots & \vdots\\ [\mathrm{S}]_{\mathrm{G}0} & [\mathrm{S}]_{\mathrm{G}1} & \cdots & [\mathrm{S}]_{\mathrm{GG}}\end{pmatrix} \times \begin{pmatrix}[\phi]_0\\ [\phi]_1\\ \vdots\\ [\phi]_{\mathrm{G}}\end{pmatrix} + \begin{pmatrix}[\mathrm{q_e}]_0\\ [\mathrm{q_e}]_1\\ \vdots\\ [\mathrm{q_e}]_{\mathrm{G}}\end{pmatrix}. \quad [6]$$

The goal is to solve for the angular flux groups, given by $[\psi]_G$. Shift couples SCALE continuous-energy (Shift MC solver) and multigroup physics (Shift MC solver and Denovo deterministic solver) cross section libraries for hybrid transport. The CPM Calculator photon sources discretized in Denovo are separable energy-space isotropic sources, which facilitate the hybrid methods. As opposed to traditional (S_n) iterative discretization methods, Denovo utilizes the Koch-Baker-Alcouffe (KBA) parallel sweep algorithm to perform a 2-D decomposition of a 3-D cartesian orthogonal structured spatial mesh (i.e., the simulation problem space) to solve the steady-state Boltzmann transport equation in space, angle, and energy (Evans et al., 2010). In other words, the KBA algorithm directly inverts the "L" term in Eq. 6 to obtain a more computationally efficient solution of the angular flux by "sweeping" through the 3-D cartesian orthogonal structured spatial mesh, as opposed to traditional source iteration techniques that may take longer converge. The defined 3-D mesh in Shift is decomposed into computational domain blocks defined by the user that scale with the number of processors, as shown below (Evans et al., 2010):

$$P_I = \frac{I}{I_b}; \quad P_J = \frac{J}{J_b}; \quad B_K = \frac{K}{K_b}, \qquad [7]$$

where,
(P_I, P_J) = number of processors in the x and y directions

B_K = number of blocks in the z direction on each domain

The I, J, and K terms represent the total, global number of cells in the *x*-, *y*-, and *z*-direction respectively. The I_b,J_b, and $K_b$terms represent the size of each *x*-, *y*-, and *z*-domain on each processor, which are defined by the user. The number of "small blocks" previously mentioned in §2.2 that discrete ordinates methods visualize in the phase space to transport particles, denoted by I, J, and K are automatically calculated. The KBA decomposition may be visually depicted by Figure 2:

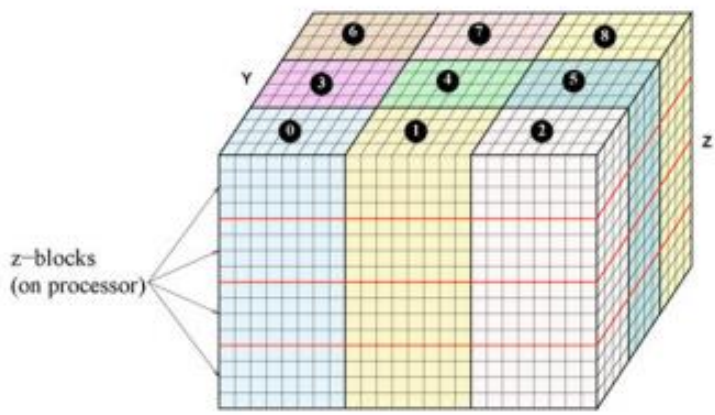

Figure 2. Decomposition of 3-D mesh for KBA. In this example, the grid is decomposed on nine processors.
The red lines (thick gray lines) indicate computational blocks in the z direction. Each processor has $I_b \times J_b \times K$ cells, and each block has size $I_b \times J_b \times K_b$ (Evans et al., 2010).

It should be noted that great care should be taken when defining the Denovo spatial mesh; a coarse mesh may result in unreliable importance maps even when source biasing is implemented. The Denovo deterministic solver also utilizes a ray tracing method to generate track-length contributions (i.e., mean free path determinations) within the geometry of the problem; increasing the number of rays fired per computational domain block (mesh face) is particularly useful for large problems with small tally volumes. This is especially prevalent with the 0.5x1 and 1x1-inch detector CPM Calculator simulations.

2.2.2. CADIS Hybrid Method Overview

The hybrid capabilities of Shift are particularly useful for speeding up the transport of sources that undergo significant attenuation in large problem geometries, as well as lowering the uncertainty associated with tally results when compared to analog (no variance reduction) MC. Shift is

currently capable of neutral particle transport for only photons and neutrons and may be used to simulate select tallies that mirror those included in MCNP, such as average flux in a volumetric cell (F4 tally in MCNP). The hybrid methodology utilized in this study is known as the CADIS (Consistent Adjoint Driven Importance Sampling) hybrid method, which is a single tally region optimization method that relies on the discrete ordinates deterministic solver, Denovo, to generate an adjoint flux and associated importance map for particles simulated in a given environment. Once the adjoint flux and importance map are generated, particles are more likely to be born in regions of higher importance in the simulation environment. Omnibus code is used to couple the Denovo deterministic and Shift MC solver as part of the Exnihilo code suite to accelerate the Shift transport simulations. The CADIS hybrid method is known to be nearly 100,000 times more efficient than analog MC based on tally figure of merit (FOM) comparisons (Wagner et al., 2011).

In the CADIS method, particles are biased (increasing the number of sampled particles in order to decrease uncertainty). The biased source distribution is utilized such that particles are more likely to contribute to the total detector response and fall within the initial statistical weights (quantifies the tally contribution of particles in a simulation environment) generated from Denovo. The biased source distribution relationship is represented by Eq. 8 and 9 (Wagner et al., 2011):

$$R = \iint q(\vec{r}, E\,)\,\phi^{+}(\vec{r}, E\,)d\vec{r}dE\ . \qquad [8]$$

where,

R = Total detector response (i.e. final tally result)
$q(\vec{r}, E)$ = Unbiased source
$\phi^{+}(\vec{r}, E)$ = Scalar adjoint flux

$$\hat{q}(\vec{r}, E) = \frac{\phi^{+}(\vec{r}, E\,)q(\vec{r}, E)}{R} \qquad [9]$$

where,

$\hat{q}(\vec{r}, E)$ = Biased source

In the CADIS hybrid method, a weight window technique is applied by generating detailed space- and energy-dependent importance parameters (particle weights) and applying geometric splitting/roulette and energy splitting/roulette, while simultaneously controlling weight variations as a particle travels throughout an environment (Wagner et al., 2011). The deterministic Denovo solver generates the adjoint flux and associated weight window map; the Shift MC solver employs the stochastic splitting/roulette method in the phase space to determine the final contribution of particles in a tally region. The initial statistical weight of a particle is, $w_0(\vec{r}, E)$, is defined by Eq. 10 (Wagner et al., 2011):

$$w_0(\vec{r}, E) \equiv \frac{q(\vec{r}, E)}{\hat{q}(\vec{r}, E)} = \frac{R}{\phi^{+}(\vec{r}, E)} \qquad [10]$$

Upon initiation of the Shift MC solver, if a particle falls below a given weight in the importance map (3-D distribution of $w_0(\vec{r}, E)$), then the particle will be split (source biasing) or rouletted (terminated) in order to sufficiently increase its weight. This hybrid technique greatly increases the rate at which the Shift MC solver final solution converges, and thus significantly increases computational efficiency.

3. METHODOLOGY

3.1. Overview

The goal of the validation effort is to simulate a detector count rate that would be normalized to an activity concentration on the surface area or in a volumetric depth of the media of interest for use in the CPM Calculator. The MCNP v6.2 radiation transport code has been utilized for validation modeling of the CPM surface calculator by simulating the energy deposition (F8) pulse height tally (Werner et al., 2017). A benchmark of Shift capabilities conducted by TAMU with the assistance of the Shift development team in December 2019 indicated that radiation transport of photons through contaminated volumetric depths, as required in the Volume CPM function, supersedes capabilities of MCNP by at speed factor of 10 for simulations of track length estimate of cell flux. The ability to conduct rapid, high-fidelity radiation transport simulations is paramount for this initiative given the initial SOW request for 23,120 discrete simulations for a series of contamination depths, 19 monoenergetic photon energies, 17 gamma-ray emitting radionuclides, and four NaI(Tl) detector models summarized in Table 3. The number of required simulations in Table 3 has been revised due to some requested depth thicknesses exceeding four mean free paths (infinite thickness) in certain media, which is described further in §4.2. It was, therefore, identified as unnecessary to conduct volumetric depth simulations in which the requested volumetric depth exceeded the infinite thickness.

Table 3. Breakdown of simulation runs required to obtain CPM detector response data (per initial SOW).

	Monoenergetic Energies	Radionuclide Energies	Contamination Depths	Detector Distances	Number Detectors	Total Runs
Concrete	19	17	7	5	4	5,320
Drywall	19	17	4	5	4	3,040
Glass	19	17	4	5	4	3,040
Soil	19	17	7	5	4	5,320
Steel	19	17	7	5	4	5,320
Wood	19	17	5	5	4	3,800
TOTAL						23,120

Primary gamma-ray emissions were alone considered from the list due to Shift's capability to conduct neutral particle, and not charged particle transport. Since Shift currently does not support a pulse height tally, a detector response function to generate detector count rates was developed by TAMU and verified by ORNL's Shift code developers in the Reactor and Nuclear Systems Division (RNSD). Any primary or secondary charged particle transport requires the use of MC code (e.g. MCNP). Therefore, beta emissions from the list of radionuclides, as well as pure beta-emitters (^{3}H and ^{90}Sr) and their associated bremsstrahlung emissions cannot be run using Shift and

were therefore not addressed in this simulations of this project, and confirmed by ORNL. In order to eliminate the computational runtime of simulating the gamma-ray emitting radionuclides in MCNP, an interpolation method developed by TAMU and independently validated by ORNL was employed. In addition, both ^{220}Rn and ^{222}Rn lack the criteria described in §4.2 for photon emission and have also been eliminated from the SOW list of detectable gamma-ray emitters. These criteria reduce the list of Superfund radionuclides of interest to the gamma-ray emitting radionuclides. In the following sections, the project tasks are outlined to describe the main components that were addressed during the performance period along with the project completion status. Detailed descriptions of the MCNP/Shift detector response function, radionuclide interpolation, and CPM Calculator final result normalization methodologies are provided. Additionally, a flow chart is provided in Figure 3 to summarize the methodology approach taken by TAMU.

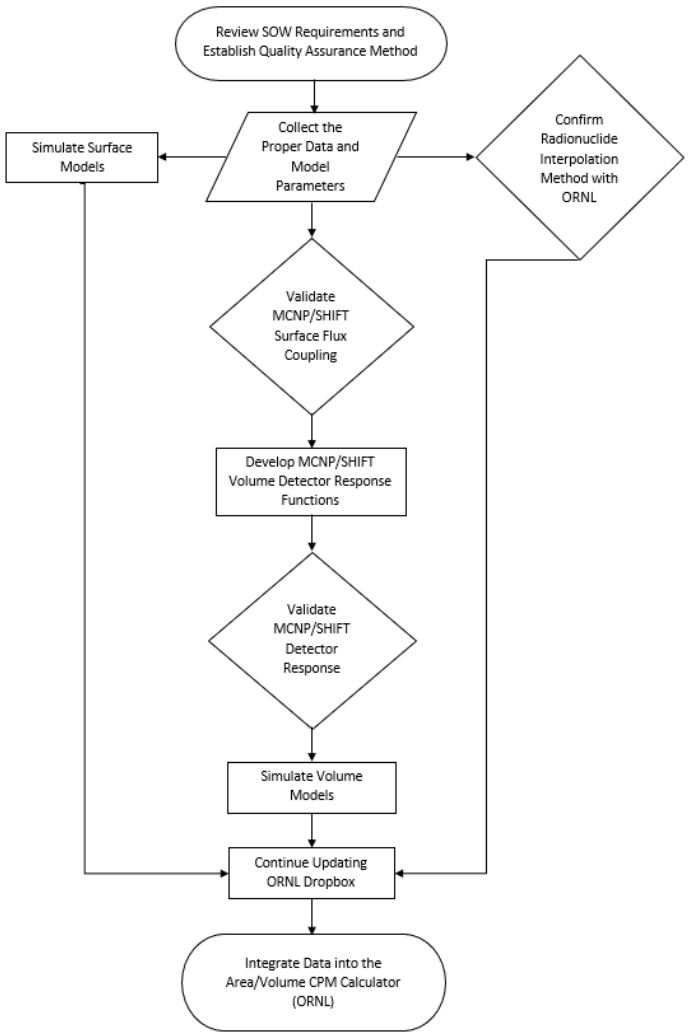

Figure 3. A flow chart that summarizes the project methodology.

3.2. Project Task Descriptions and Completion Status

3.2.1. Task Descriptions

Task I: Quality Assurance Project Requirements

The first task in the actuation of this project involved the development of a quality assurance strategy between TAMU and ORNL. This was initiated through the development of a file naming and inventory system, housed in an ORNL-provided Dropbox account. In addition to the PI (Dewji), key personnel in this work include Mr. Ethan Asano (TAMU), whose expertise in Shift and MCNP was leveraged for the simulation work and Python expertise was also leveraged for automating the creation of simulation files and post-processing of simulation results; Mr. David Coleman (TAMU), whose expertise in Python was harnessed for implementing the radionuclide interpolation method, as well as secondary quality assurance of all data and model inputs and outputs post-processing; and Mr. Alexander Perry (TAMU), who assisted in the project effort by simulating MCNP and Shift files provided by Mr. Asano, as well as optimizing Python scripts provided by Mr. Asano. As the methodology described herein has been vetted with ORNL, whose key personnel over the contract period provided QA confirmation for detector models, materials simulations, and radionuclide interpolation. These interactions have been documented in the Monthly Status Letter Reports provided to ORNL throughout the contract period.

Task II: Data and Model Parameter Definition

The second task in the actuation of this project involved the establishment of key data and model parameters that were employed in the construction of environmental contamination models. This included the compiling and formatting of radionuclide emission energies and associated emission probabilities, environmental material definitions, and source geometry definitions (depth and radii) for use in radiation transport simulations (Shift and MCNP). The key data and model parameters are provided in Appendix A.

Task III: MCNP/Shift Coupling Surface Validation

To fully harness the computational efficiency advantages of Shift, notably with volumetric contamination scenarios, benchmarks were established to demonstrate that the average cell flux reaching the detector from an environmental contamination source in Shift was equivalent to the value in MCNP for discretized energy bins. Benchmark results are reported in §4.3.

Task IV: MCNP/Shift Detector Response Function Development

As Shift's capabilities are currently limited to accelerating transport to estimate average cell flux reaching the detector, where energy deposition tallies are not possible, a pulse height energy deposition tally using MCNP was created for 19 monoenergetic reference fields to develop a detector response model for each of the four NaI(Tl) detectors. This first step in the process entailed the development of a representative detector in MCNP for each of the 0.5x1-, 1x1-, 2x2-, and 3x3-inch NaI(Tl) detectors using detector model schematics, given in Figures 4-7. The second step was to develop a reliable, consistent relationship between an MCNP F8 pulse height tally and

average cell flux in order to convert a Shift average cell flux value to an “MCNP-equivalent” pulse height for any given volumetric contamination simulation. The detailed methodology is described in §3.3.

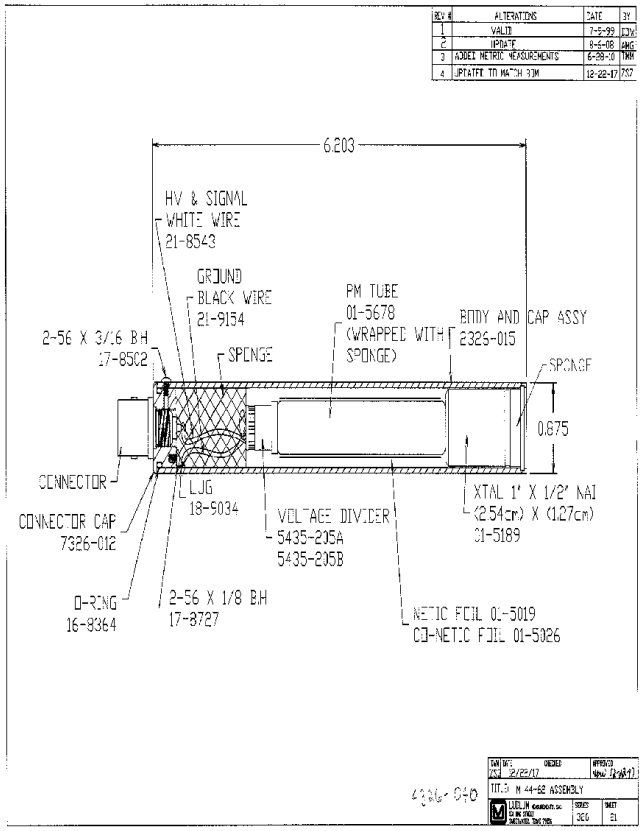

Figure 4. Ludlum Model 44-62 0.5x1 NaI(Tl) schematic line diagram (Ludlum Measurements Inc., 2020).

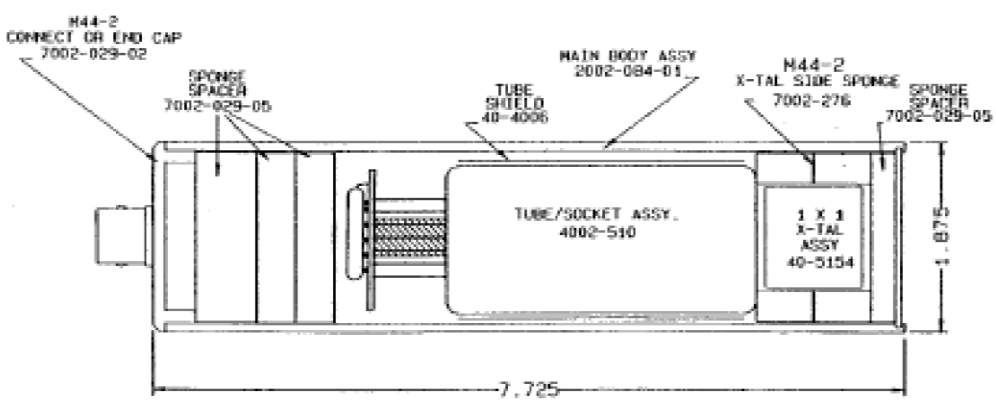

Figure 5. Ludlum Model 44-2 1x1 NaI(Tl) schematic line diagram (Ludlum Measurements Inc., 2020).

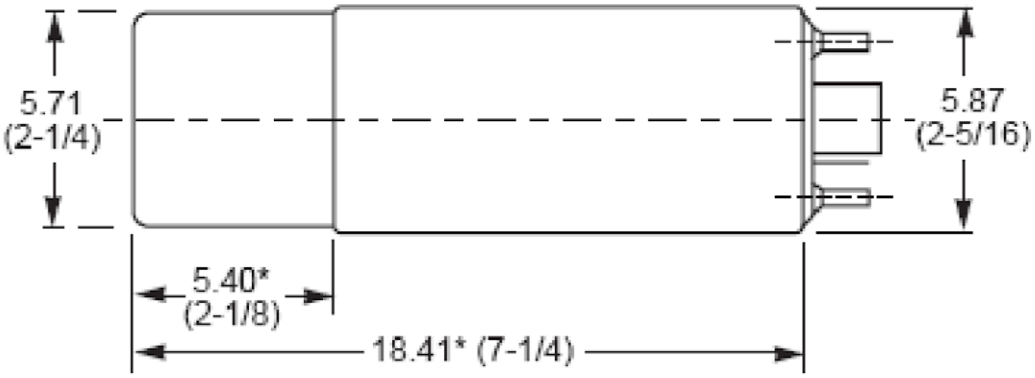

Figure 6. Canberra/Mirion Model 802-2 NAIS 2x2 Na(Tl) schematic line diagram (Mirion Technologies, 2020).

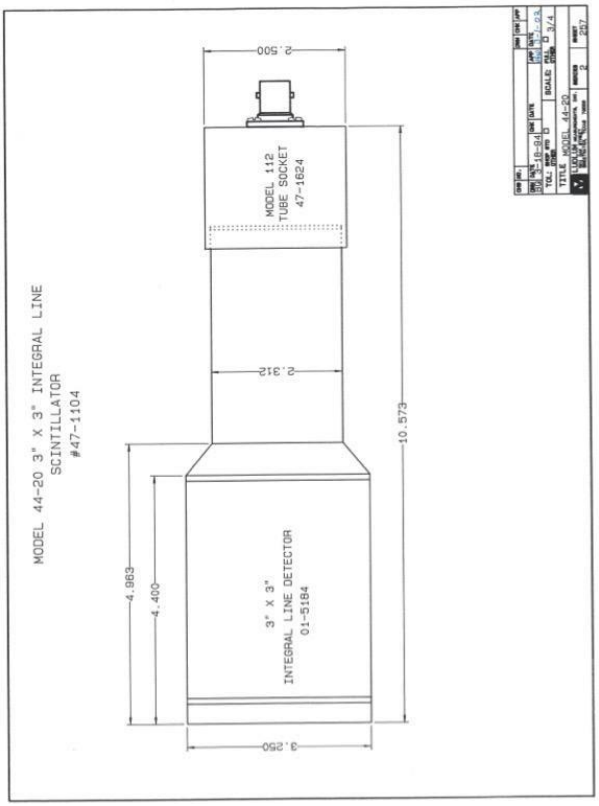

Figure 7. Ludlum Model 44-20 3x3 NaI(Tl) schematic line diagram (Ludlum Measurements Inc., 2020).

Task V: Detector Response Function Validation

Validation using the CADIS hybrid method of Shift for radiation transport through environmental media and coupling the binned response with the MCNP/Shift response function developed in

Task IV were validated against MCNP pulse height deposition models for the analogous environmental media contamination. Sample results are reported in §5.

Task VI: Surface CPM Simulations

Source definitions, environmental geometry, and subsequent detector responses for the MCNP surface contamination runs were simulated in the RNSD Romulus and Remus clusters at ORNL. Python codes to automate setup of the environmental media geometry, gamma-ray source definitions, and detector response post-processing were prepared to actuate the surface contamination simulations. All final MCNP F8 pulse height tally results are to be reported with relative errors of less than 5%.

Task VII: Volume CPM Simulations

Source definitions, environmental geometry, and subsequent average cell fluxes for the Shift volumetric contamination runs were simulated in the RNSD Apollo cluster at ORNL. Python codes to automate setup of the environmental media geometry, gamma-ray source definitions, and post-processing of average cell fluxes to obtain the detector responses were prepared to actuate the volumetric contamination simulations. All final Shift average cell flux tally results are to be reported with relative errors of less than 5%.

Task VIII: Radionuclide CPM Simulations

Detector responses from the discrete Superfund radionuclides of interest in accordance with Table 5 in §4.2 have been requested. A method developed by ORNL has been employed to eliminate computational runtime for the surface and volumetric contamination runs; this approach for the CPM project was implemented after consultation with ORNL (Asano et al., 2020). The detailed methodology is described in §3.4. Sample results are provided in §5.

3.2.2. Completion Status

All MCNP surface contamination 2x2- and 3x3-inch detector simulations have reached proper tally convergence of less than 5%. The input/output (I/O) files have been reported to ORNL through the provided secure electronic repository on Dropbox. The remaining MCNP surface contamination 0.5x1- and 1x1-inch detector simulations are currently underway; the I/O files will be uploaded to the Dropbox accordingly upon completion.

The Shift volumetric contamination 2x2- and 3x3-inch detector simulations are complete and post-processed. The I/O files have been reported to ORNL through the provided secure electronic repository on Dropbox. The remaining Shift volumetric 0.5x1- and 1x1-inch detector simulations continue and final files uploaded to the ORNL Dropbox. Detailed spreadsheets that confirm the completion status of MCNP surface and Shift volumetric simulations are provided to ORNL and are continuously updated by TAMU (refer to electronic accompaniment for a record of file statuses).

3.3. MCNP/Shift Detector Response Methodology

3.3.1. Response Function Overview

As stated prior, MCNP was used to simulate all surface contamination validation scenarios. All media of interest were simulated with a surface contamination layer equal to one micron (0.0001 cm). MCNP is able to generate lower tally relative errors for surface contamination simulations when compared to Shift under the same modeling conditions; however, Shift is still able to achieve proper convergence in a faster process. Nevertheless, the MCNP surface contamination results proved to be very useful in developing a reliable, consistent relationship between the F8 pulse height and Shift average flux tally for any given CPM volume calculator modeling scenario. An important relationship between the energy-dependent fluence and any tally of interest may be introduced by the following equation (X-5 Monte Carlo Team, 2003):

$$C = \int \phi(E) f(E)\, dE \qquad [11]$$

where,

C = Tally of interest (i.e. pulse height)
$\phi(E)$ = Energy-dependent fluence $\left(\frac{1}{cm^2 - sp}\right)$
$f(E)$ = The product or summation of cross section library quantities or user-provided response function

This implies that the MCNP F8 pulse height tally may be approximated by multiplying the energy-fluence (the F4 average cell flux is sufficient) by a "response function" provided by the user. The response function is simply a relationship that sufficiently captures the behavior of a source (i.e., energy dependence), such that the average cell flux may be normalized by in order to obtain the tally of interest. The user-provided response function is not limited to the energy dependence of the source as shown in Eq. 11; additional dependencies such as space and angle must be accounted.

3.3.2. MCNP/Shift Response Function Implementation

Detector response functions were developed by normalizing the MCNP surface contamination pulse height by the Shift surface contamination average cell flux under the same modeling conditions for each of the 19 monoenergetic energies of interest. The response functions are therefore the MCNP pulse height per Shift unit flux ratios. In total, there were 120 response function groups (each with 19 different values as a function of energy), comprising six contaminated media, four detector configurations, and five source-detector distances. The MCNP F8 pulse height tallies represented the "full model" (i.e., simulations with a detector) components of the response functions. The denominator of the response functions (Shift average cell flux) was simulated under the same conditions as the "full model," but the entire detector was filled with a void. The denominator of the response functions was the Shift surface contamination average cell flux tallied over the entire detector volume filled with a void. Hence, in the Shift volumetric

contamination models, the average cell flux in a void detector was converted to a "full model" pulse height after normalizing by the appropriate response function. A VisEd representation of the response function implementation in MCNP for a 2x2-inch detector problem is shown in Figure 8 (Schwarz et al., 2011).

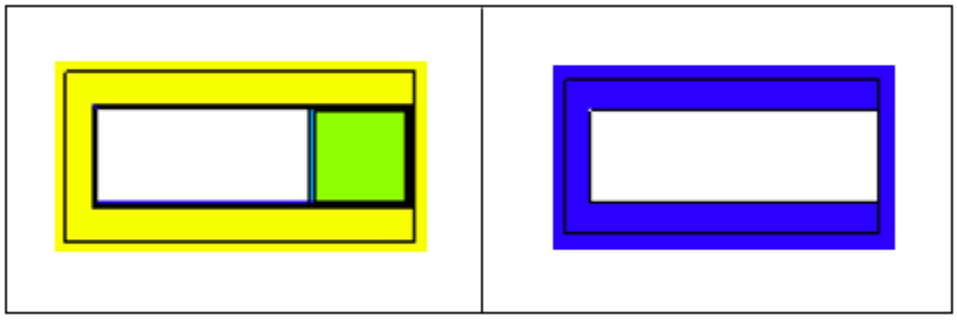

Figure 8. A full model 2x2-inch NaI(Tl) detector and corresponding void detector shown from left to right, respectively.
Each detector model is housed in a universe filled with air. The full model surface response (MCNP pulse height) in the detector crystal (green region) is divided by the corresponding Shift surface average cell flux in the void detector region (white) to create a response function.

The MCNP/Shift response function is given by the following:

$$RF_i(pulse - cm^2) = \frac{\left(\frac{pulse}{sp}\right)_{Full,i}}{\left(\frac{1}{cm^2 - sp}\right)_{Void,i}} \qquad [12]$$

where,

RF_i = Response function for a specific contaminated medium, detector configuration, source-detector distance, and energy bin, *i*;

$\left(\frac{pulse}{sp}\right)_{Full,i}$ = MCNP "full model" surface contamination F8 pulse (count) per source particle (sp) at energy bin, *i*; and

$\left(\frac{1}{cm^2 - sp}\right)_{Void,i}$ = Corresponding Shift surface contamination average cell flux in a void detector at energy bin, *i*.

The final Shift volumetric detector response is calculated as follows:

1. A Python script reads the MCNP F8 pulse height and Shift surface average cell flux tally results for each of the 19 monoenergetic energies. The pulse height tallies are divided by the average cell flux tallies for each energy bin.
2. The Python script reads the Shift volumetric contamination average cell flux values and corresponding energy bins (1024 bins emulating a multi-channel analyzer) from 0 to 3 MeV.
3. The Python script interpolates over the 19-energy response function group in step (1) for each of the Shift energy bins described in step (2) to obtain the detector response function (RF_i) at each energy bin.
4. The Python script finally multiplies each of the energy-binned Shift volumetric average cell flux values by the corresponding detector response function and sums up each value to obtain the final detector response.

The final detector response relationship is shown by Eq. 13:

$$Response = \sum_{i=1}^{1024} \begin{pmatrix} Average\ Cell\ Flux \\ in\ a\ Void\ Detector \end{pmatrix}_i (RF)_i \qquad [13]$$

where,

Response = Shift final detector response $\left(\frac{pulse}{sp}\right)$

$\begin{pmatrix} Average\ Cell\ Flux \\ in\ a\ Void\ Detector \end{pmatrix}_i$ = Shift volumetric contamination average cell flux in a void detector; for a specific contamination medium and depth, detector configuration, source-detector distance, and energy bin, *i*; and

$(RF)_i$ = Response function at energy bin, *i*.

3.3.3. Weight Window Automation Method

When the CADIS hybrid method in Shift is simulated, a massive .h5 file that stores the importance map (weight windows) of the problem is generated. Each time that a CADIS hybrid method problem is simulated, a varying amount of computational runtime is required for Denovo to generate the importance maps for the problem. The developers of Shift at ORNL developed a method for automating importance map implementations in the CADIS hybrid simulations in order to eliminate redundancies associated with the generation of importance maps. This method was implemented in the CPM project after consultation with ORNL (Asano et al., 2020). The weight window automation method may be implemented if the geometry, materials, and location of a single tally region in the problem is constant; therefore, the single tally optimization CADIS hybrid method may be compatible.

The initial weight windows (importance maps) are a function of space and energy across the problem geometry as shown by Eq. 10 (Wagner et al., 2011). The initial weight windows that comprise the importance maps will be equal for any source energy spectrum and contamination depth, so long as the contaminated medium type, detector configuration, and source-detector

distance are constant. The Shift volumetric contamination source is therefore interpolated over the surface contamination source expected contribution to the detector response (pulse height), or the biased source distribution given by Eq. 9 (Wagner et al., 2011). The weight window automation method works by simulating a CADIS hybrid method problem with 1 particle at any energy and contamination depth for the contaminated medium type, detector configuration, and source-detector distance of interest. The .h5 file containing the aforementioned importance map may be automatically loaded into the Shift volumetric contamination problems within a response function group. This results in 120 .h5 files being generated (120 response function groups), as opposed to thousands (one for each simulation).

3.4. Radionuclide CPM Simulation Methodology

In order to eliminate a massive amount of computational runtime, a method developed at ORNL was utilized to determine the pulse height for radionuclide surface and volumetric contamination CPM Calculator simulations. In order to determine the pulse height for a given radionuclide, the detector response of each of the 19 monoenergetic energies (as a function of media type, source-detector distance, and detector configuration) was obtained. A Python script was created to read in the detector response data at those 19 monoenergetic energies. Using a piecewise cubic hermite interpolating polynomial, detector responses were interpolated from this data at the energies of the given radionuclide. The resulting pulse heights at these energies were multiplied by the intensity of the corresponding photon being emitted, and the summation of these emissions gave the pulse height for a given radionuclide. For the surface contamination simulations, the MCNP F8 pulse height tallies were interpolated over (120 groups each with 19 energies). For the volumetric contamination simulations, the detector responses obtained from the methodology described in §3.3.2. were interpolated over. The radionuclide volumetric contamination interpolation groups varied as a function of contamination depth for each of the 19 energies (inclusive of media type, source-detector distance, and detector configuration).

On December 1st, 2020, ORNL and TAMU confirmed validation of the CPM radionuclide interpolator, where energies below 20 keV are to be removed from the interpolator, given that the NaI detector Ludlum models of interest only detect photons as low as 20 keV (20 keV threshold for 1x1-inch., 60 keV for 0.5x1-, 2x2-, 3x3-inch.). It was also decided that the F8 results from the interpolator are to be summed without normalizing to the total emissions probability. This ensures that the final results are inclusive of only emissions that are used in the interpolator. All emissions that have an intensity of less than 0.1% were included in the interpolator, assuming an energy > 20 keV.

3.5. Normalization of Final Results for Use in CPM Calculator

3.5.1. CPM Area Calculator Activity to CPM Conversion Factor

The MCNP/Shift detector responses generated from TAMU will be normalized as follows to obtain the ith monoenergetic or radionuclide area activity to CPM conversion factor:

$$CF_i\left(\frac{cpm}{\frac{pCi}{cm^2}}\right) = \left(\frac{pulse}{Bq-s}\right)\left(\frac{60\ sec}{min}\right)\left(\frac{Bq}{27.027\ pCi}\right)\binom{Source}{Area} \qquad [15]$$

The activity to CPM conversion factor was calculated by normalizing the MCNP F8 pulse height or Shift detector response by the contaminated source area and converting to minutes and picocuries. It should be noted that the detector response is normalized to per radionuclide decay (Bq-s). All MCNP/Shift tallies were normalized to per source particle (sp), but it may be assumed that one sp is equal to one decay if one photon is emitted per radionuclide decay. This is true for all monoenergetic tallies, as well as radionuclide tallies that are properly normalized to the sum of the intensities, or total number of photons emitted per radionuclide decay. TAMU employed Python scripting to normalize all radionuclide outputs by the sum of intensities prior to delivery.

3.5.2. CPM Volume Calculator Activity to CPM Conversion Factor

The equation below was previously used to calculate the activity to CPM conversion factor. The MCNP energy fluence per source particle was converted to a CPM reading normalized to the activity concentration in the medium of interest.

$$CF_i\left(\frac{cpm}{\frac{pCi}{g}}\right) = (82.7)\binom{Source}{Area}\binom{Source}{Dept}\binom{Source}{Dens}\left(\frac{e}{\bar{w}_{air}}\right)(S_{det}) \times \left\{(dfrac_i)\left[\sum_{photons}(Y)\left(\sum_C(\varphi_E)\left(\frac{\mu_{en}}{\rho_{air,E}}\right)(RF_{det,E})\right)\right]\right\} \quad [16]$$

The MCNP/Shift detector responses generated from TAMU were normalized as follows to obtain the ith monoenergetic or radionuclide area activity to CPM conversion factor:

$$CF_i\left(\frac{cpm}{\frac{pCi}{g}}\right) = \left(\frac{pulse}{Bq-s}\right)\left(\frac{60\ sec}{min}\right)\left(\frac{Bq}{27.027\ pCi}\right)\binom{Source}{Area}\binom{Source}{Depth}\binom{Source}{Dens} \quad [17]$$

Contrary to the previous conversion method employed by the older generation of CPM, normalizing to the detector sensitivity (S_{det}), mass energy absorption coefficient $\left(\frac{\mu_{en}}{\rho_{air,E}}\right)$, and detector response factor ($RF_{det,E}$) is not required. The TAMU detector response output needs only to be normalized to the contamination volume and density and converted to minutes and picocuries. As with the area activity to cpm conversion factors, TAMU employed in-house Python scripting to normalize all radionuclide outputs by the sum of intensities prior to delivery.

4. BENCHMARK RESULTS

4.1. Materials Data

In this project, source data was obtained from the report published by Pacific Northwest National Laboratory, "PIET-43741-TM-963 PNNL-15870 Rev. 1 Compendium of Material Composition Data for Radiation Transport Modeling" and summarized in MCNP syntax in Table A1 in Appendix A (McConn et al., 2011). The exception is for the material definition of soil, which was taken from the Environmental Protection Agency's Federal Guidance Report 15 silty soil composition (Veinot et al., 2017). From older generation CPM simulations conducted prior to

TAMU's effort, inputs for material definitions were identified by TAMU as incorrect for four of the six environmental media, where weight fraction data was incorrectly defined as atom fraction data, making any prior files unusable for any QA or other utility for the following CPM Calculator media: concrete, soil, steel, and drywall.

4.2. Emission Definition

Source emissions for gamma-ray emitting radionuclides outlined in the SOW were obtained from International Commission on Radiological Protection (ICRP) Publication 107 (ICRP, 2008) through NRC/ORNL's Radiological Toolbox software. Per communication with ORNL on 06/01/2020, the highest energy gamma-ray emission was selected as the basis upon which to simulate depth contamination and define the radius of the wide-area contamination plane. Four mean free paths represent a transmission of 1.8% of photons in good geometry. Table A.2 in Appendix A summarizes the mass attenuation coefficients and densities for each of the environmental media needed to compute the mean free path of the highest energy emission from the identified radionuclide, and define the depth of contamination as four mean free paths (Hubbell et al., 1996; Berger et al., 2010). Table A.3 in Appendix A summarizes the mass attenuation coefficients and densities for each of the environmental media needed to compute the mean free path of the discrete monoenergetic emissions, and define the depth of contamination of infinite thickness as four mean free paths (Hubbell et al., 1996; Berger et al., 2010). The source emissions energies and probabilities are provided as an electronic supplement in the ORNL Dropbox.

The contamination thicknesses requested to be modeled are summarized in the SOW in Table 1. However, the mass attenuation coefficient, and hence infinite thickness, varies as a function of photon energy, which may exceed the infinite thickness for the requested volumetric depth thickness of contamination. The five rightmost columns ("1cm depth", "2 cm depth", etc.) in Table A.2 and A.3 in Appendix A indicate whether the simulation thickness requested in the SOW is less than 4 mean free paths as a function of energy. Regions highlighted in green indicate the depth thicknesses of contamination that are less than 4 mean free paths; however, regions highlighted in red indicate requested depth thicknesses that exceed 4 mean free paths; regions in white were not requested for simulation per Table 1. Per detector, this affects 39 simulations (total 156) in the radionuclide source energies and 37 discrete energy simulations per detector (total 148) in the discrete energy simulations. Finally, Table A.4 defines the radii of the contamination plane representative of 4 mean free paths for a photon to travel in air, representative of an infinite plane. The plane radii will vary as a function of discrete energy simulated (Table A.3) or highest radionuclide emission energy (Table A.2).

4.3. Preliminary F4 Benchmarks for Exterior Coupling Surface

Preliminary average cell flux tallies (F4) were obtained over a void box for 50 keV, 100 keV, 500 keV, 1 MeV, and 3 MeV monoenergetic sources buried within 1 cm of contaminated soil in Shift and MCNP. The source-detector distance for all runs was 10 cm; however, limiting source radii and world boundary dimensions were chosen for the purpose of demonstrating the convergence of Shift and MCNP physics methods for tallying average cell flux, which were eventually converted to pulse height. The results of the F4 convergence test is shown in Table 4. The default lower energy cutoff in Shift is 10 keV; therefore, a 10 keV energy cutoff was employed in MCNP. It

should be noted that in the production simulations, the Shift lower energy cutoff was specified at 1 eV (equivalent to MCNP). It was determined that Shift and MCNP F4 values under the same modeling conditions converge well as shown in Table 4. The preliminary results suggest that under the same modeling conditions the detector response in Shift is expected to converge well with MCNP when converting average cell flux to pulse height at each interpolated energy bin. A comparison of the MCNP and Shift F4 distribution over each energy spectrum is shown in Figures 9-13.

Table 4. Results of the preliminary F4 convergence tests.

Energy (MeV)	MCNP F4 (mean)	Relative Error	Shift F4 (mean)	Relative Error	Percent Error
0.05	8.237(-5)	1.000(-3)	8.240(-5)	1.191(-3)	0.035%
0.1	1.213(-4)	8.000(-4)	1.212(-4)	8.529(-4)	0.036%
0.5	1.343(-4)	7.000(-4)	1.346(-4)	8.072(-4)	0.169%
1	1.282(-4)	8.000(-4)	1.279(-4)	8.180(-4)	0.230%
3	1.194(-4)	8.000(-4)	1.176(-4)	8.493(-4)	1.505%

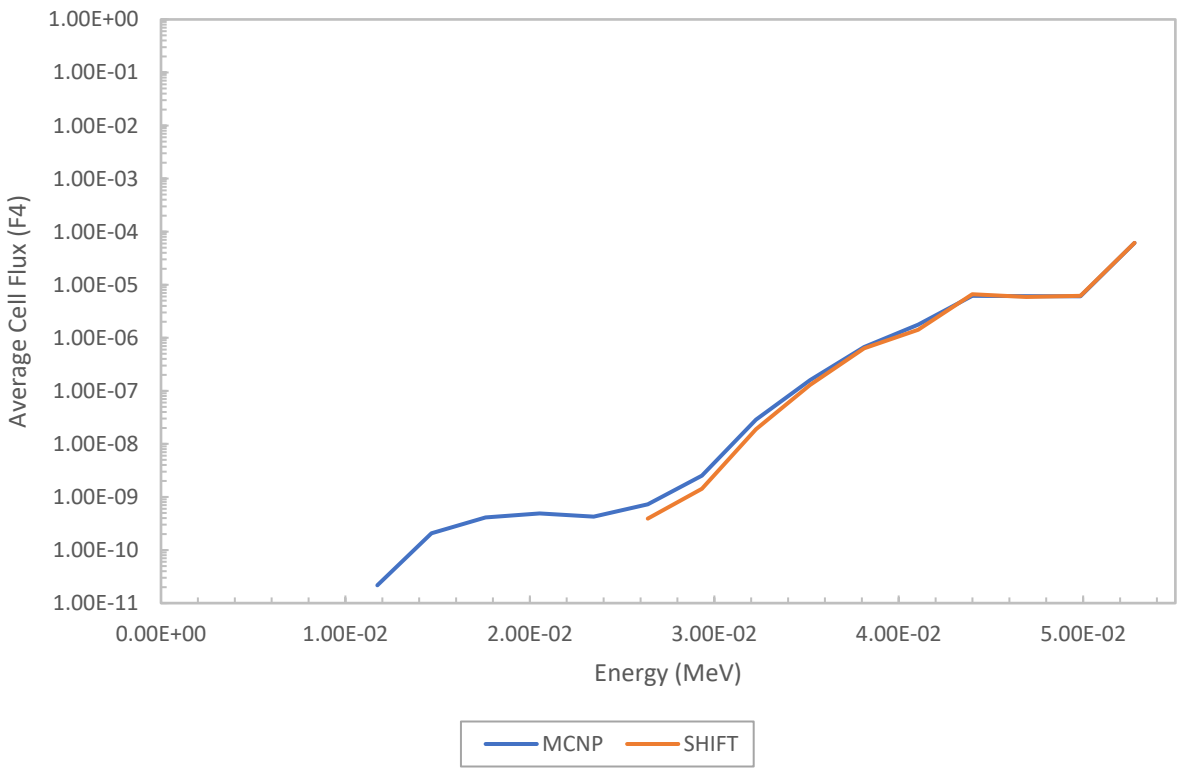

Figure 9. F4 comparison over the 50 keV spectrum.

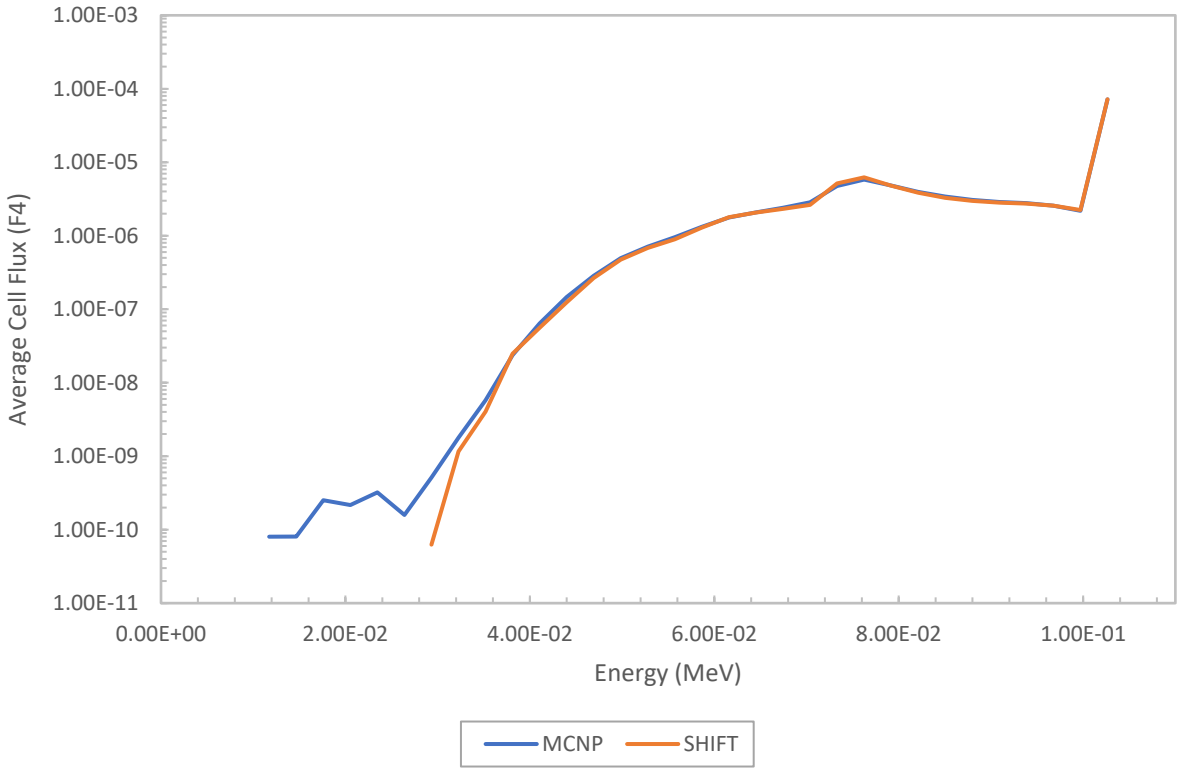

Figure 10. F4 comparison over the 100 keV spectrum.

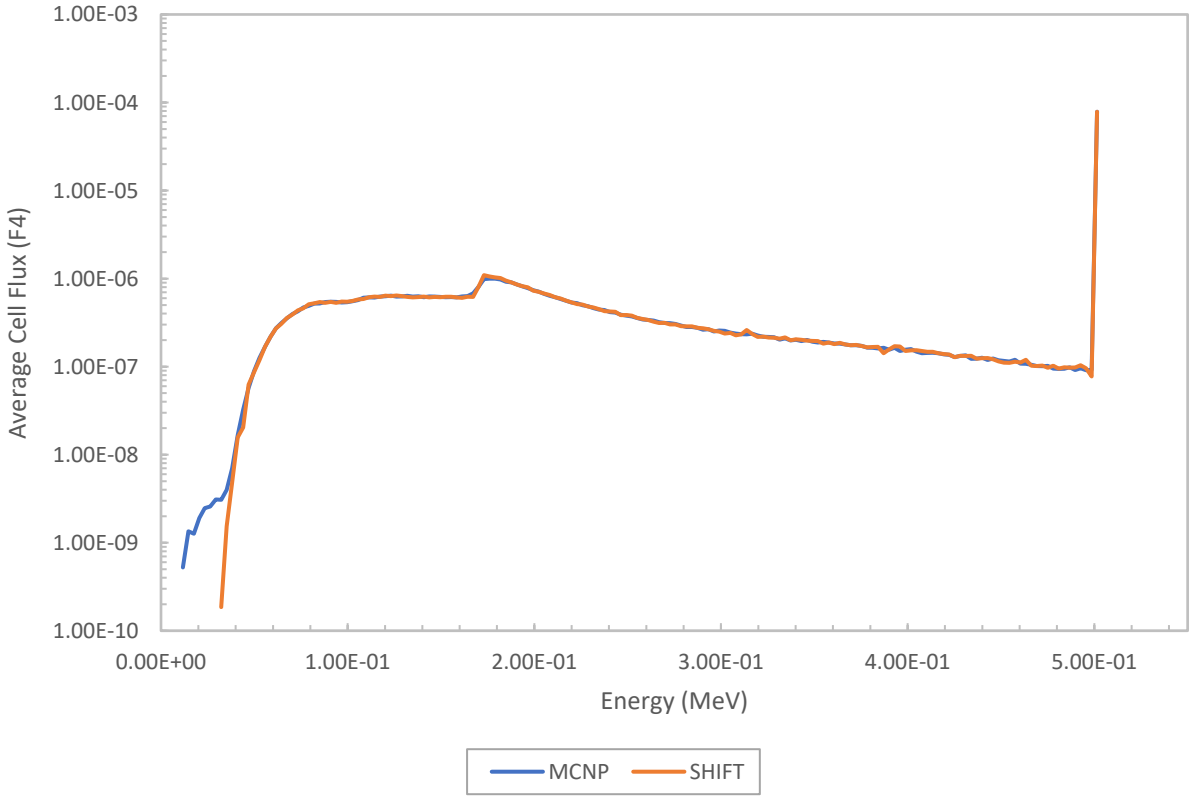

Figure 11. F4 comparison over the 500 keV spectrum.

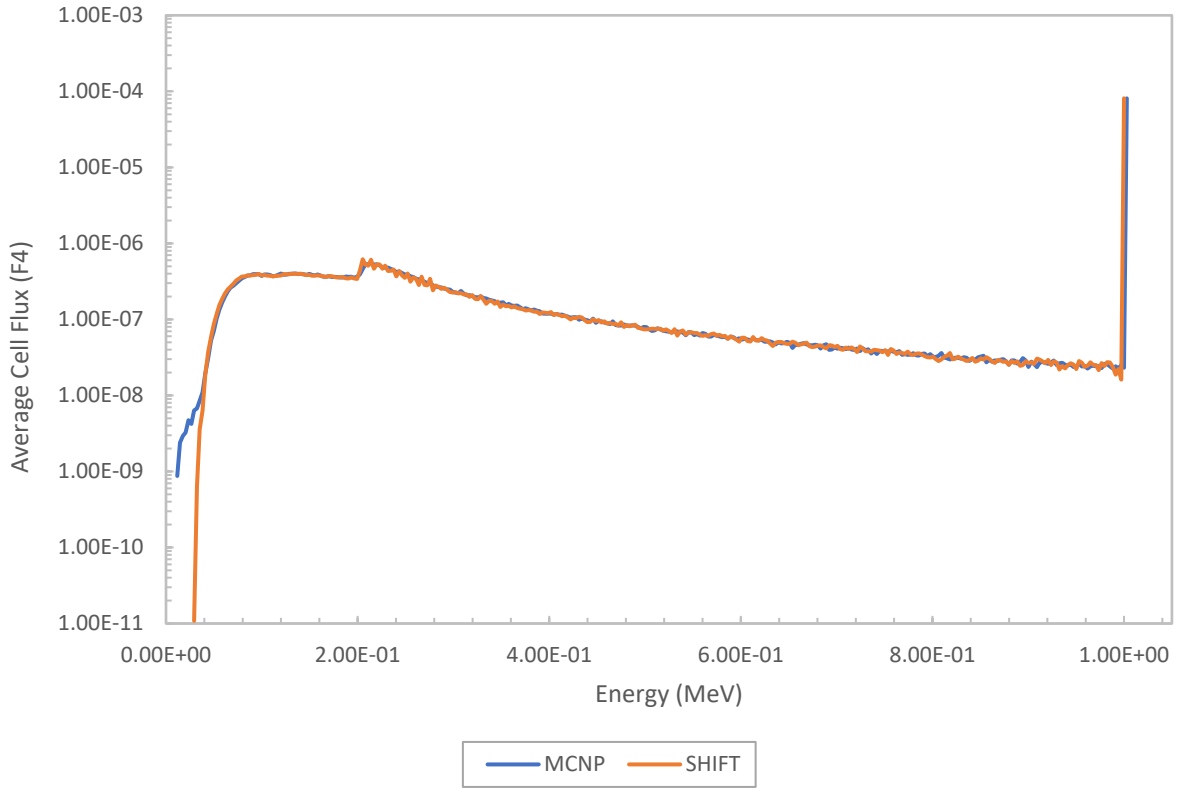

Figure 12. F4 comparison over the 1 MeV spectrum.

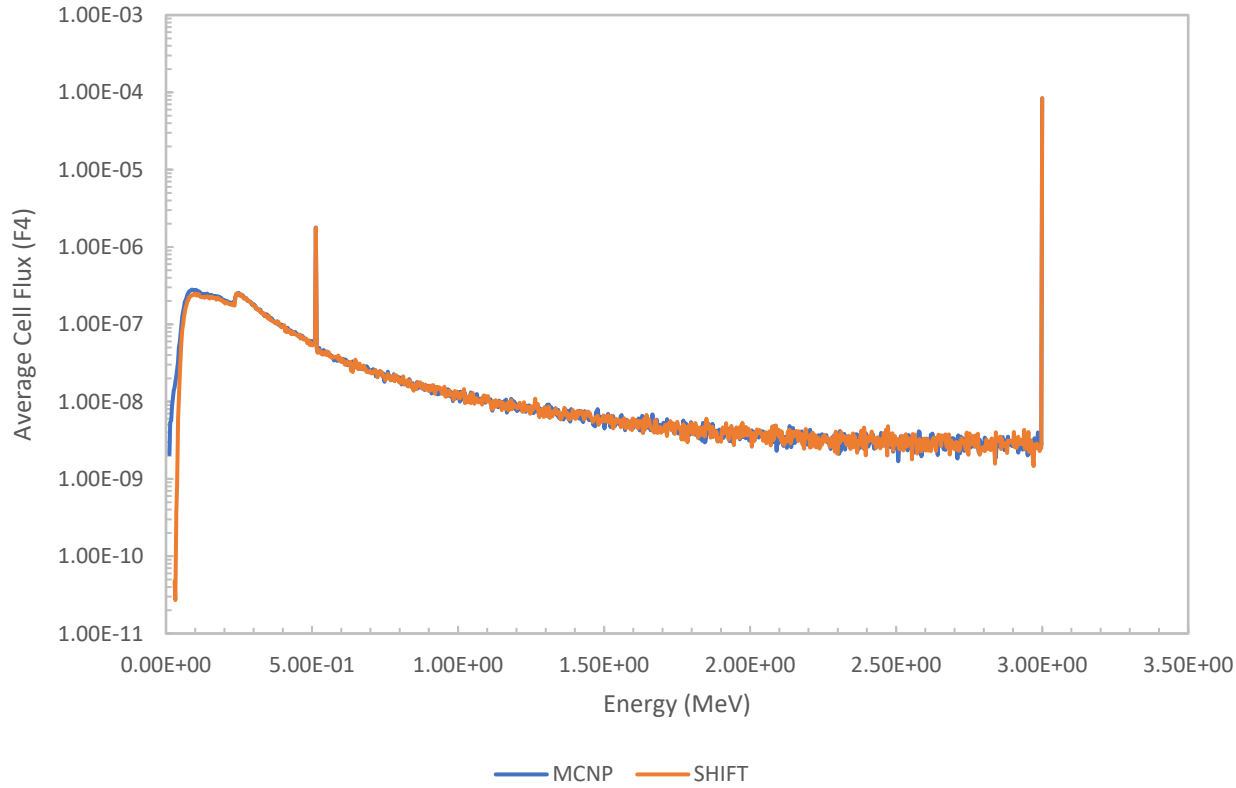

Figure 13. F4 comparison over the 3 MeV spectrum.

5. RESULTS AND DISCUSSION

Surface and volumetric detector responses (as a function of energy) are described for sample monoenergetic simulations and radionuclide interpolations. The majority of results are reported for soil, as it was determined to be the highest priority CPM Calculator contaminated medium after discussion with ORNL. Results for the 2x2- and 3x3-inch detectors are provided (status described in §3.2.2) and per the identified and prioritized runs identified by ORNL. It should be noted that results for all energies in the volumetric contamination section are initially reported for completion; results for low energy simulations may not be reliable due to recommended contamination depths exceeding four mean free paths (infinite) in a medium as described in §4.2.

5.1. Monoenergetic Surface Contamination

In Figures 14-15, the efficiency (i.e., detector response) is shown to decrease with increasing source-detector distance as expected. The number of isotropic photons emitted from the soil that deposit energy in the detector crystal decrease with increasing source-detector distance due to the inverse square law, where irradiance decreases in proportion to the square of the distance. The detector response will peak at around 30 keV and 70 keV for the 2x2- and 3x3-inch detectors, respectively. The efficiency will increase at lower energies due to increasing energy deposition through photoelectric effect absorptions in the detector crystal, and will begin to decrease as less photons are absorbed and Compton scattering interactions become more prevalent. This efficiency threshold is lower for the 2x2-inch detector when compared to the 3x3-inch detector, due to the 3x3-inch detector having a larger geometric efficiency allowing it to capture more higher energy photons before Compton scattering becomes more prevalent. Pair production may also overlap with Compton scattering when the energy reaches at least 1.022 MeV. After the detector response reaches a peak, it will continue to decrease as the energy increases due to more photons scattering away from or through the detector crystal without depositing energy.

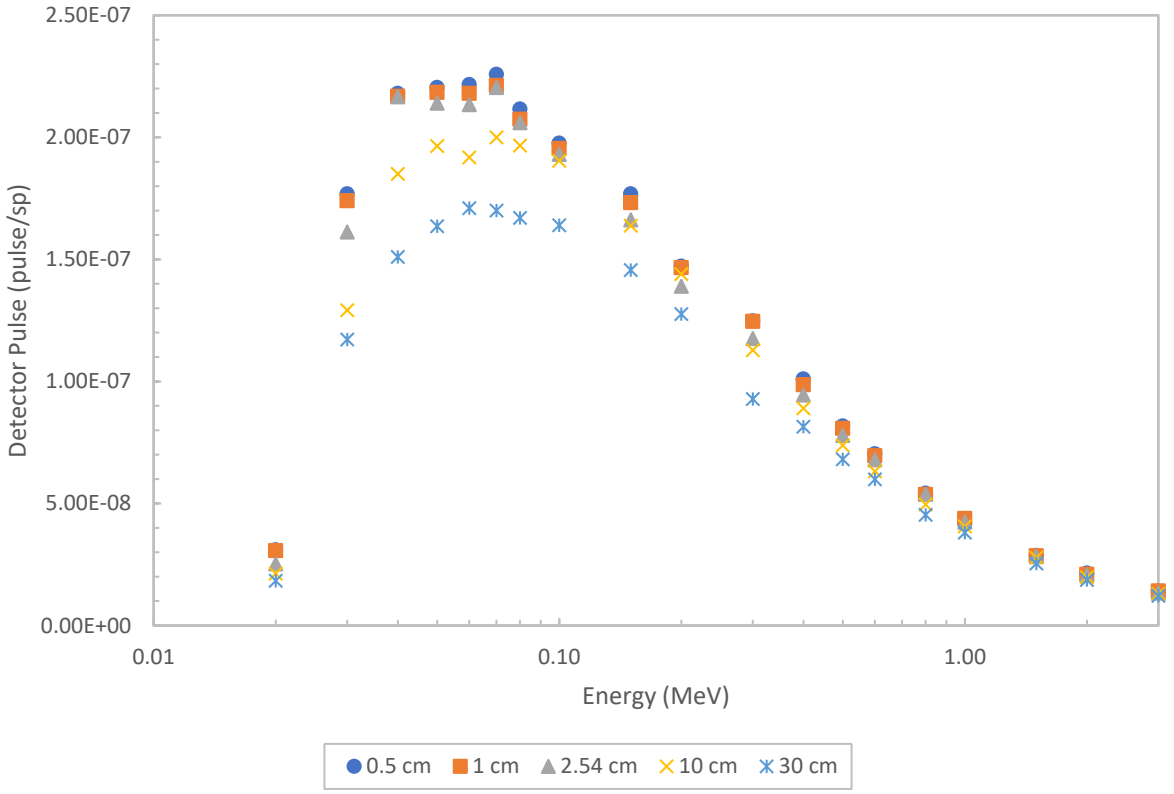

Figure 14. Soil surface contamination 3x3-inch detector response as a function of energy for all requested source-detector distances.

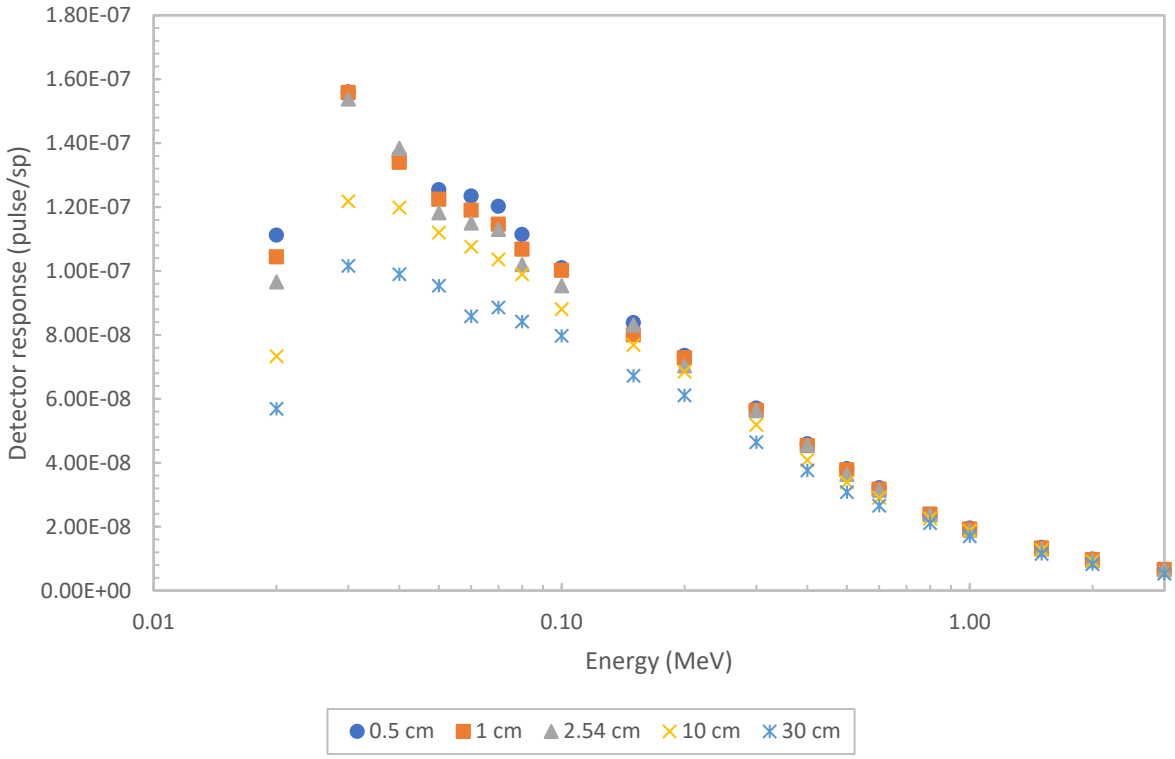

Figure 15. Soil surface contamination 2x2-inch detector response as a function of energy for all requested source-detector distances.

The detector responses for the 3x3- and 2x2-inch detectors in Figures 16-17, respectively, will as the densities and path lengths of the contaminated media increase; therefore, wood will consistently have the highest detector response, whereas steel will have the lowest. The volume of all contaminated media (with the exception of infinite depths) will be the same at each energy; media with higher densities will have larger masses and will therefore increase source attenuation prior to reaching the detector. Hence, less photons will be available to deposit energy in the detector crystal as media densities increase.

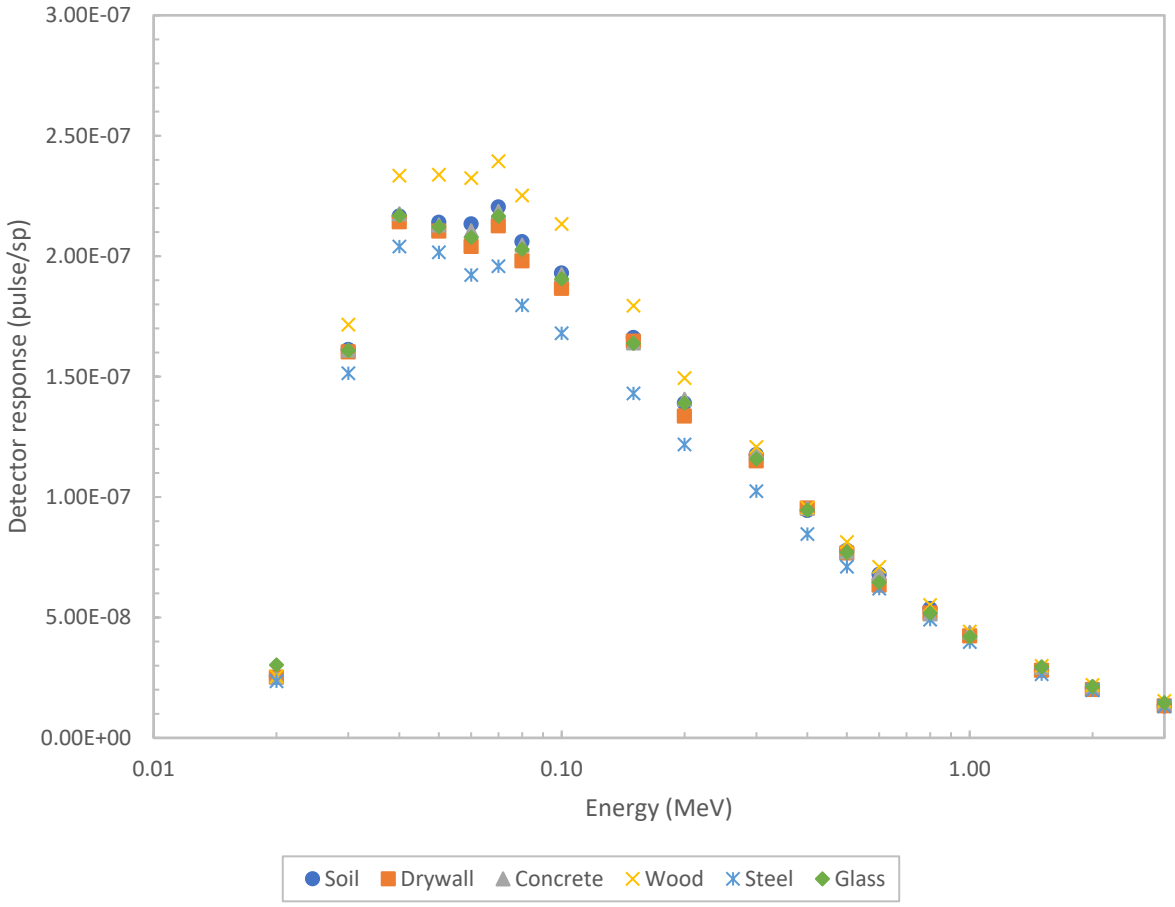

Figure 16. Surface contamination 3x3-inch detector response as a function of energy for all requested media (source-detector distance of 2.54 cm).

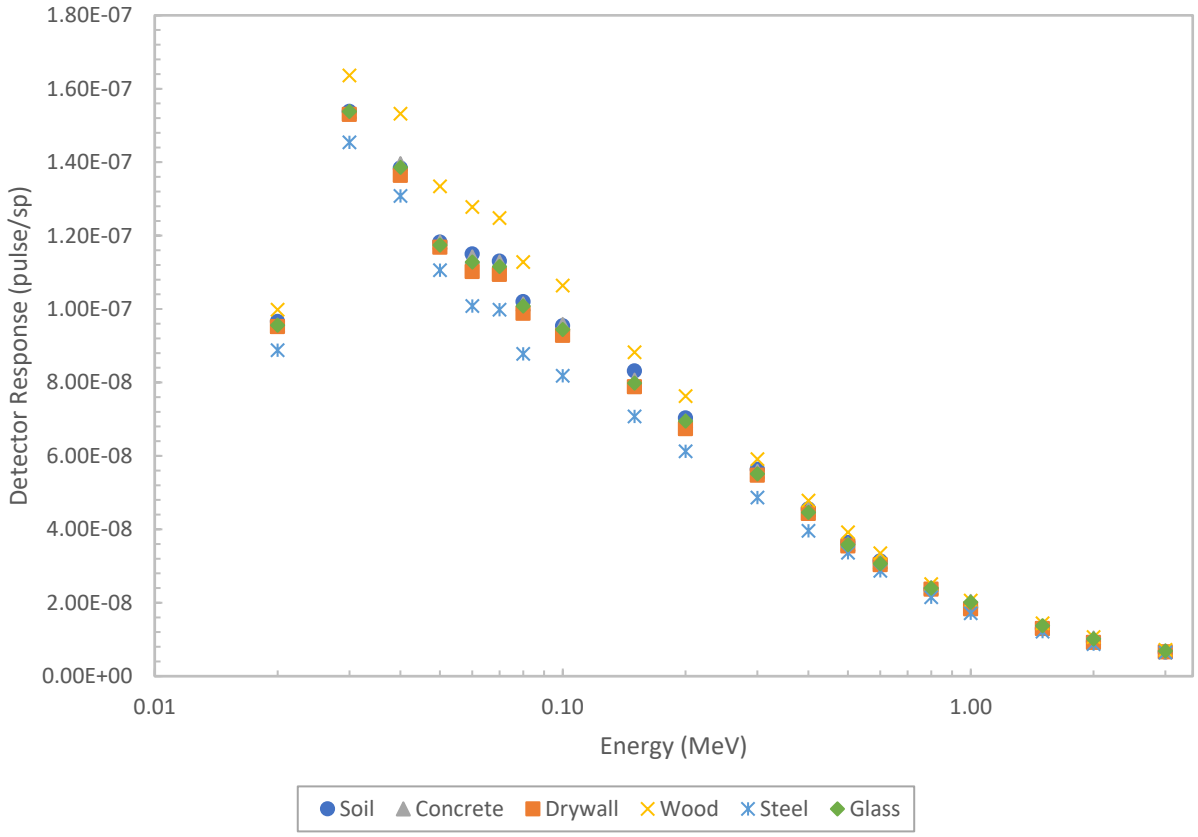

Figure 17. Surface contamination 2x2-inch detector response as a function of energy for all requested media (source-detector distance of 2.54 cm).

5.2. Monoenergetic Volumetric Contamination

The detector response will decrease as the contamination depth increases for the 3x3- and 2x2-inch detectors, as shown by Figures 18-19. The infinite depths are not constant; the infinite depths are defined as 4 mean free paths in the contaminated medium of interest as a function of the source energy. As a result, the infinite depth may be higher or lower than the requested discrete contamination depths, which result in altered trends seen in Figures 18-19. As expected, the detector response will increase with decreasing contamination depth, since a larger source distribution (flux) will be available to interact with the detector crystal.

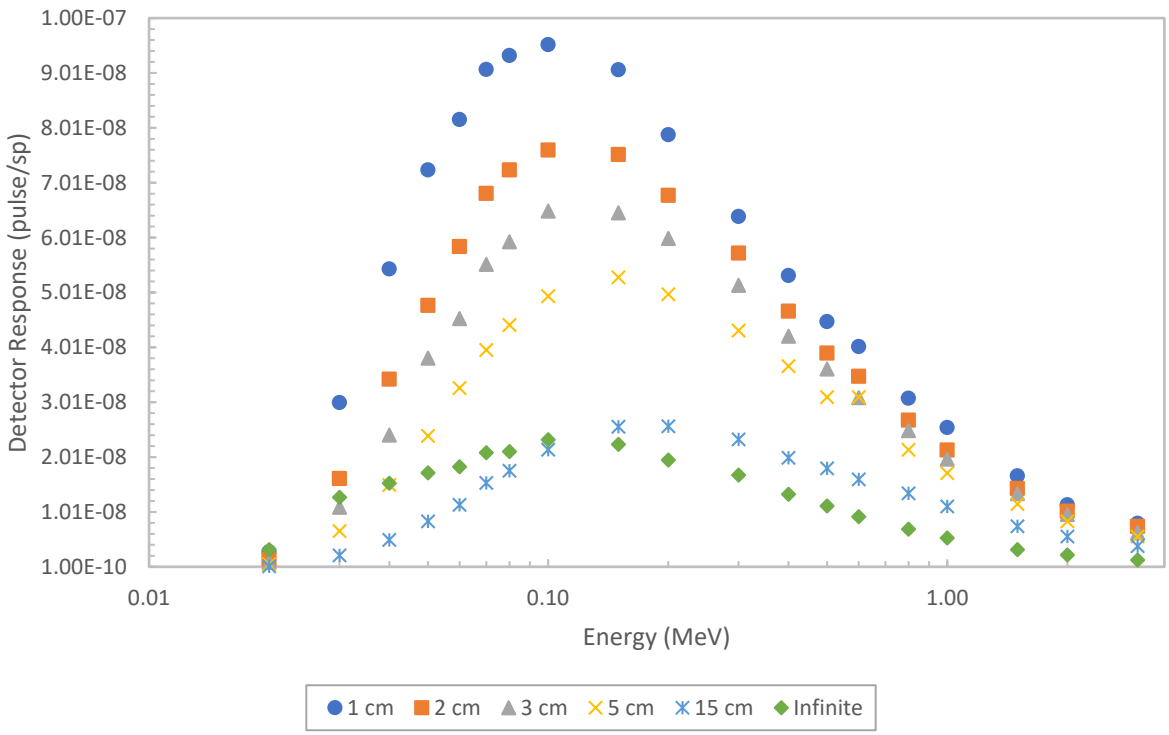

Figure 18. Soil volumetric contamination 3x3-inch detector response as a function of energy for all requested volumetric contamination depths (source-detector distance of 2.54 cm).

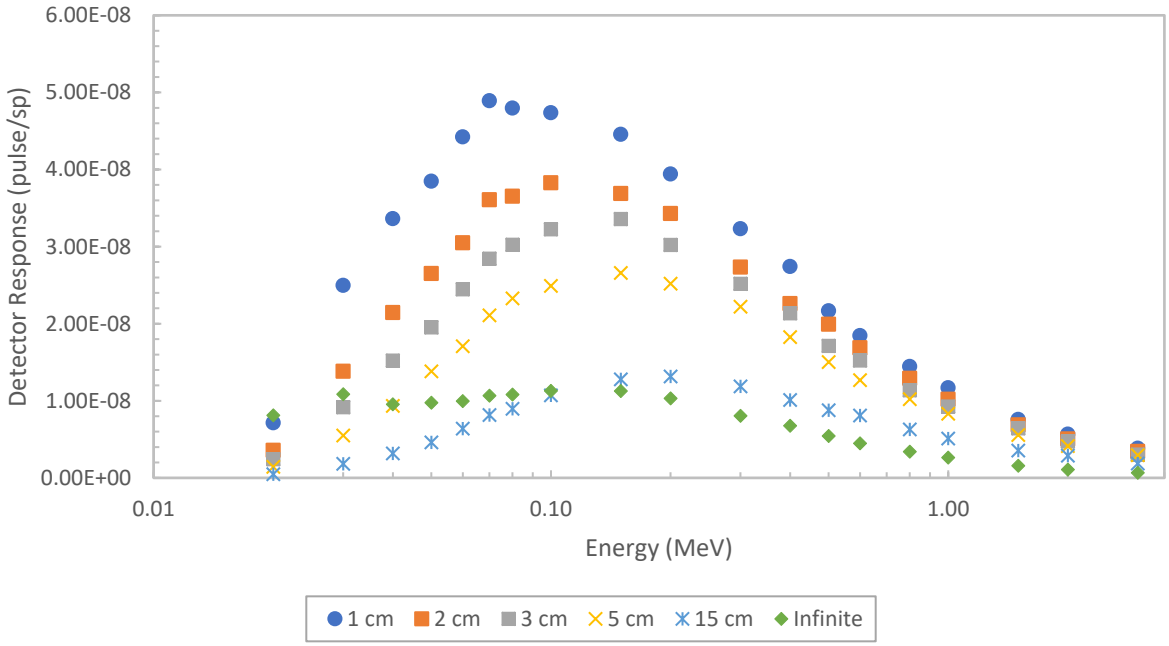

Figure 19. Soil volumetric contamination 2x2-inch detector response as a function of energy for all requested volumetric contamination depths (source-detector distance of 2.54 cm).

The 3x3- and 2x2-inch detector responses in Figures 20-21 display the equivalent trends shown in Figures 16-17 with respect to increasing (or decreasing) contaminated media densities. It should be noted that a significantly large spread exists between steel and wood akin to the surface contamination values in Figures 16-17. This may be explained by the differences in angular dependencies between the surface and volumetric sources. The buried sources become more heavily attenuated following emission, as previously described, and will therefore vary more significantly with respect to direction throughout the problem environment. Therefore, photons emitted from steel may be more anisotropic when compared to wood due to having more photon buildup where the collided flux increases. In contrast, the difference in photon buildup experienced between steel and wood would not be as significant for the isotropic source since less attenuation in each medium would occur.

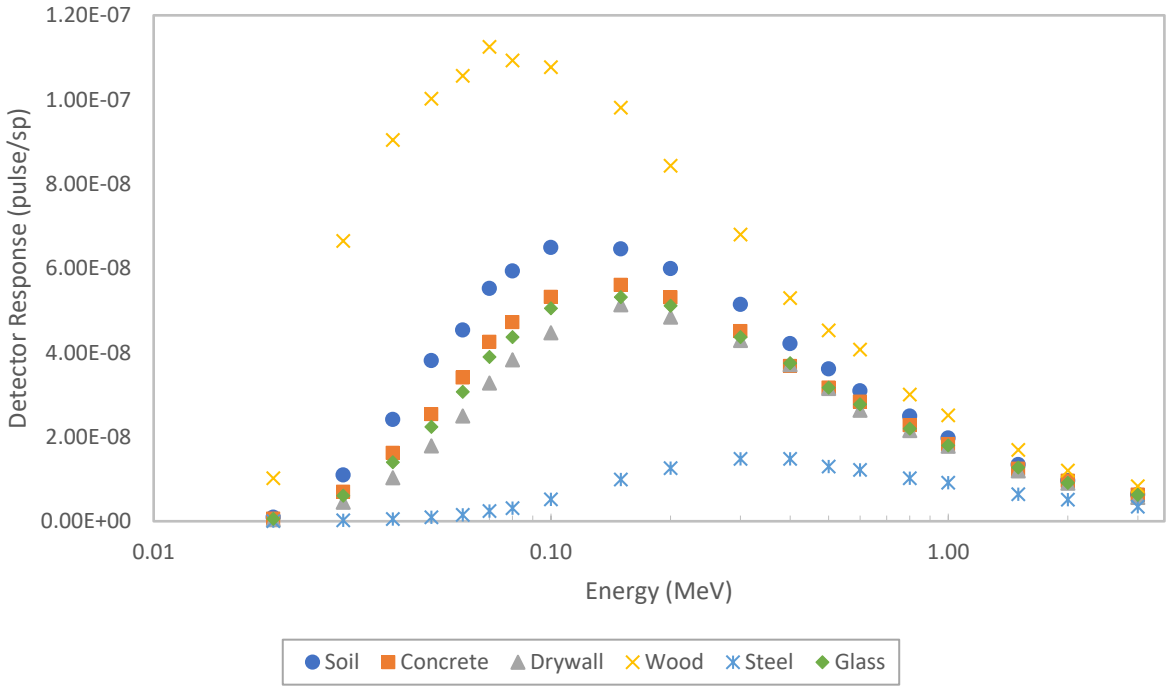

Figure 20. Volumetric contamination (depth of 3 cm) 3x3-inch detector response as a function of energy for all requested media (source-detector distance of 2.54 cm).

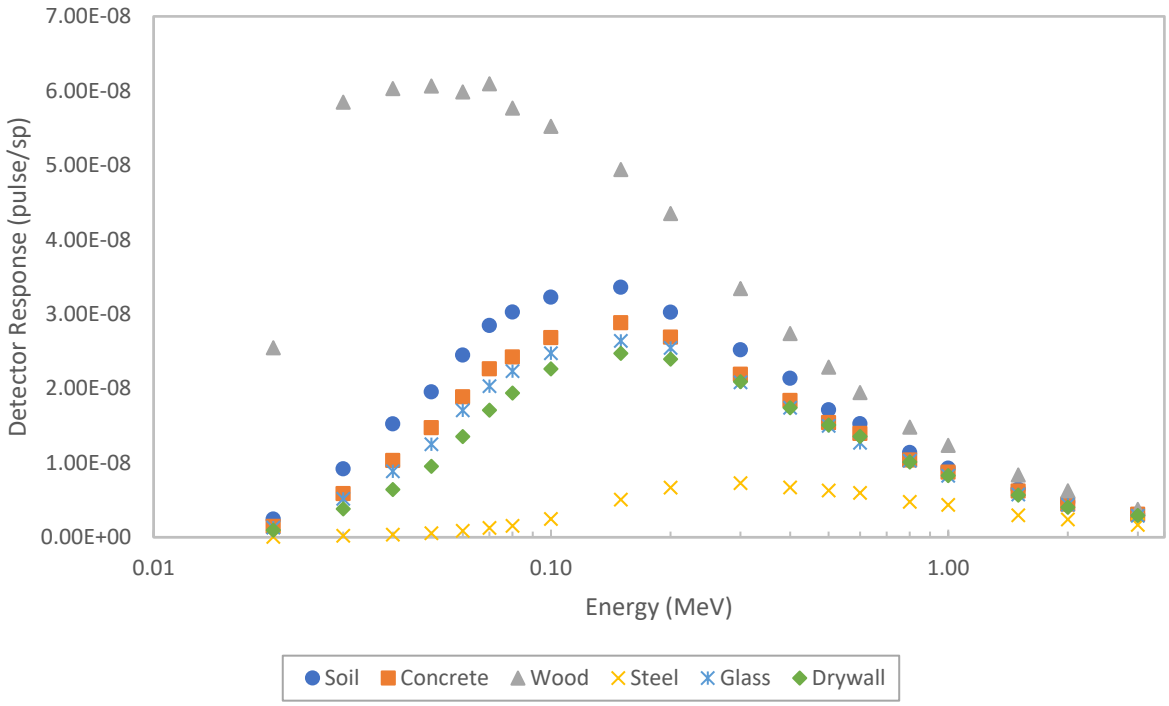

Figure 21. Volumetric contamination (depth of 3 cm) 2x2-inch detector response as a function of energy for all requested media (source-detector distance of 2.54 cm).

Table 5. Sample MCNP/Shift volumetric contamination full model comparisons.

Media	Energy (MeV)	Depth (cm)	Detector	Distance (cm)	MCNP Response (pulse/sp)	Shift Response (pulse/sp)	Percent Error
Soil	1.0	15	3x3-inch	30	1.07(-8)	1.06(-8)	1.32%
Concrete	0.5	3	2x2-inch	2.54	1.63(-8)	1.54(-8)	5.56%
Drywall	0.1	1	2x2-inch	1	3.76(-8)	3.92(-8)	4.36%
Steel	0.8	5	3x3-inch	0.5	7.23(-9)	7.04(-9)	2.62%

Sample comparisons between MCNP full model pulse height simulations and Shift detector response interpolations are shown in Table 5. The MCNP pulse height values had relative errors of less than 5%. Currently, the Shift interpolated detector response values are given without associated uncertainties; the convergence criterion for volumetric contamination simulations are based upon the Shift average cell flux relative errors (less than 5%). The results for MCNP and Shift demonstrate relatively well convergence with equivalent magnitudes. This is especially significant given the differences in radiation transport methods used (stochastic and hybrid) for simulating the requested large problem geometries accompanied with small tally volumes.

5.3. Radionuclide Interpolation

Sample results for radionuclides of common concern following a release or contamination scenario (nuclear powerplant accident, radiological dispersal device, etc.) are provided for the 3x3- and 2x2-inch soil detectors as a function of depth are given in Tables 6-7. ICRP Publication 107 energy and intensity values at 20 keV or above were interpolated over using the method described in §3.4.

Table 6. Sample soil 3x3-inch detector response results for radionuclides of high concern in emergency response/dose assessment as a function of depth (source-detector distance of 2.54 cm).

Depth	Radionuclide Detector Response (pulse/sp)		
	^{137m}Ba-137/^{137}Cs	^{131}I	^{238}U-238/^{234m}Pa
Surface	7.03(-8)	1.11(-7)	2.01(-9)
1 cm	3.62(-8)	5.85(-8)	1.04(-9)
2 cm	3.05(-8)	5.09(-8)	8.49(-10)
3 cm	2.69(-8)	4.55(-8)	7.49(-10)
5 cm	2.69(-8)	3.92(-8)	6.09(-10)
15 cm	1.38(-8)	2.09(-8)	3.24(-10)
Infinite	8.57(-9)	1.50(-8)	2.43(-10)

Table 7. Sample soil 2x2-inch detector response results for radionuclides of high concern in emergency response/dose assessment as a function of depth (source-detector distance of 2.54 cm).

Depth	Radionuclide Detector Response (pulse/sp)		
	^{137m}Ba-137/^{137}Cs	^{131}I	^{238}U-238/^{234m}Pa
Surface	2.97(-8)	4.59(-8)	8.54(-10)
1 cm	1.74(-8)	3.03(-8)	5.08(-10)
2 cm	1.51(-8)	2.47(-8)	4.18(-10)
3 cm	1.34(-8)	2.30(-8)	3.65(-10)
5 cm	1.11(-8)	1.97(-8)	3.01(-10)
15 cm	6.95(-9)	1.07(-8)	1.57(-10)
Infinite	4.46(-9)	7.67(-9)	1.24(-10)

The interpolation method employed at TAMU was validated through technical collaboration efforts with ORNL. It is recommended that TAMU and ORNL reach a consensus for comparing the interpolated results with full (direct) MCNP radionuclide pulse height simulations to further validate the method employed.

6. CONCLUSIONS AND FUTURE WORK

Detector response functions using MCNP/Shift were developed in order to simulate thousands of volumetric contamination problems in Shift that would otherwise take years to complete using traditional analog MC. The results have proven to converge well with full MCNP pulse height simulations, and exhibit reliable trends. The radionuclide interpolation method validated through technical collaboration efforts with ORNL will eliminate the need for expending excess amounts of computational resources in the event the CPM Calculator list of radionuclides expands in the future. It is recommended that TAMU and ORNL reach a consensus for comparing the interpolated results with full MCNP radionuclide pulse height simulations to further validate the method employed.

Given the timeframe of performance period and the capabilities of Shift and MCNP to conduct transport simulation models for the vast number of required simulations, bremsstrahlung interactions for the beta emitters was not included in this SOW. However, TAMU strongly recommends to ORNL that the bremsstrahlung component to CPM be addressed in future work and that TAMU has all capabilities to continue with this simulations immediately upon completion of the SOW tasks for primary gamma-emission detector responses. The accuracy of the CPM Calculator is valid only for these primary gamma emissions and may be underestimate in the absence of bremsstrahlung contributions in specific contamination scenarios.

Furthermore, it must be noted that the response functions generated here do not replace required experimental validation of detector responses, as computational simulation tools do not permit the real simulation of detector response due to dead time, gain shift, and pulse-pile up effects.

All 3x3- and 2x2-inch detector surface and volumetric contamination results have reached proper convergence and are currently being post-processed in preparation for delivery to the shared

ORNL Dropbox. The 1x1- and 0.5x1-inch detector models for surface and volumetric contamination are currently being simulated until proper convergence is achieved. TAMU will continue to update the shared ORNL Dropbox as the final results continue to be updated. Upon completion of the CPM Calculator modeling project, or throughout the ongoing effort thereof, TAMU desires to collaborate with ORNL for the production of a technical manuscript (TM) and associated peer-reviewed journal and conference publications describing the project and its applications in facilitating field sampling techniques.

7. ACKNOWLEDGMENTS

The TAMU Radiological Engineering, Detection and Dosimetry (RED²) Laboratory CPM modeling project affiliates would like to thank Dr. Gregory Davidson (ORNL), Dr. Douglas Peplow (ORNL), Dr. Cihangir Celik (ORNL), and Caleigh Samuels (ORNL) for their provided technical expertise throughout the project effort.

8. REFERENCES

ASANO, E., COLEMAN, D. December 1 2020. RE: Personal Communication. Type to SAMUELS, C., DOLISLAGER, F.

ASANO, E., September 25 2020. RE: Personal Communication. Type to DAVIDSON, G.

BERGER, M., HUBBELL, J., SELTZER, S., CHANG, J., COURSEY, J., SUKUMAR, R., ZUCKER, D. & OLSEN, K. 2010. XCOM: Photon cross sections database, NIST Standard Reference Database 8 (XGAM) [Online]. Available: https://www.nist.gov/pml/xcom-photon-cross-sections-database [Accessed 2020].

EVANS, T.M., STAFFORD, A. S., SLAYBAUGHT, R.N., CLARNO, K.T. 2010. Denovo: A New Three-Dimensional Parallel Discrete Ordinates Code in SCALE, Nuclear Technology, 171:2, 171-200, DOI: 10.13182/NT171-171.

HUBBELL, J. & SELTZER, S. 1996. X-Ray Mass Attenuation Coefficients [Online]. Available: https://www.nist.gov/pml/x-ray-mass-attenuation-coefficients [Accessed 2020].

ICRP 2008. ICRP Publication 107: Nuclear decay data for dosimetric calculations. Ann ICRP, 38, 1-26.

Ludlum Measurements Inc. https://ludlums.com/products/all-products/category/gamma-scintillator

MCCONN, R. J., GESH, C. J., PAGH, R. T., RUCKER, R. A. & WILLIAMS III, R. 2011. Compendium of material composition data for radiation transport modeling. Pacific Northwest National Lab (PNNL), Richland, WA (United States).

Mirion Technologies https://www.mirion.com/products/nais-2x2-led-temperature-stabilized-scintillation-detector

PANDAYA, T.M., JOHNSON, S.R., EVANS, T.M., DAVIDSON, G.G., HAMILTON, S.P., GODFREY, A.H. 2016. IMPLEMENTATION, CAPABILITIES, AND BENCHMARKING OF

Shift, A MASSIVELY PARALLEL MONTE CARLO RADIATION TRANSPORT CODE. Oak Ridge National Laboratory, Oak Ridge, TN 37831, USA.

SCHWARZ, A. L., SCHWARZ, R. A. & CARTER, L. L. 2011. MCNP/MCNPX Visual Editor Computer Code.

VEINOT, K. G., ECKERMAN, K. F., BELLAMY, M. B., HILLER, M. M., DEWJI, S. A., EASTERLY, C. E., HERTEL, N. E., MANGER, R. J. R. & BIOPHYSICS, E. 2017. Effective dose rate coefficients for exposure to contaminated soil. 56, 255-267.

WAGNER, J.C., PEPLOW, D.E., MOSHER, S.W., EVANS, T. M.. 2011. Review of Hybrid (Deterministic/Monte Carlo) Radiation Transport Methods, Codes, and Applications at Oak Ridge National Laboratory. Oak Ridge National Laboratory, Oak Ridge, TN 37831, USA.

WERNER, C.J. (ed.), 2017 "MCNP Users Manual - Code Version 6.2", LA-UR-17-29981.

X-5 Monte Carlo Team, “MCNP – A General N-Particle Transport Code, Version 5.” Volume I: Overview and Theory, LA-UR-03-1987 (April, 2003).

APPENDIX A. Supplemental Data

Table A.1. Definition of material composition for radiation transport simulations.

Material	ZAID	Weight Fraction
Concrete (Regular)	1000	-0.010000
	8000	-0.532000
	11000	-0.029000
	13000	-0.034000
	14000	-0.337000
	20000	-0.044000
	26000	-0.014000
Soil (FGR 15)	1000	-0.021
	6000	-0.016
	8000	-0.577
	13000	-0.05
	14000	-0.271
	19000	-0.013
	20000	-0.041
	26000	-0.011
Steel (304)	6000	-0.000400
	14000	-0.005000
	15000	-0.000230
	16000	-0.000150
	24000	-0.190000
	25000	-0.010000
	26000	-0.701730
	28000	-0.092500
Drywall (Gypsum/Plaster of Paris)	1000	-0.023416
	8000	-0.557572
	16000	-0.186215
	20000	-0.232797
Glass (Plate)	8000	-0.459800
	11000	-0.096441
	14000	-0.336553
	20000	-0.107205
Wood (Southern Pine)	1000	-0.059642
	6000	-0.497018
	7000	-0.004970
	8000	-0.427435
	12000	-0.001988
	16000	-0.004970
	19000	-0.001988
	20000	-0.001988

Table A.2. Densities and mass attenuation coefficients and infinite thickness depths for six media for gamma-emitting radionuclide emission energies.

Radionuclide	Energy (MeV)	Medium	Mass Attenuation Coefficient (cm^2/g)	Medium Density (g/cm^3)	Mean Free Path 1/μ (cm)	D 4/μ (cm)	1 cm depth	2 cm depth	3 cm depth	5 cm depth	15 cm depth
Am-241	0.0595	Soil	0.27	1.60	2.31	9.23	0	0	0	0	1
		Concrete	0.28	2.30	1.57	6.26	0	0	0	0	1
		Wood	0.19	0.64	8.03	32.10	0	0	0	0	
		Steel	1.21	8.00	0.10	0.41	1	1	1	1	1
		Glass	0.29	2.40	1.43	5.72	0	0	0		
		Drywall	0.35	2.32	1.24	4.97	0	0	0		
Co-60	1.330	Soil	0.06	1.60	11.13	44.52	0	0	0	0	0
		Concrete	0.06	2.30	7.83	31.32	0	0	0	0	0
		Wood	0.06	0.64	26.76	107.06	0	0	0	0	
		Steel	0.05	8.00	2.41	9.64	0	0	0	0	1
		Glass	0.05	2.40	7.58	30.33	0	0	0		
		Drywall	0.06	2.32	7.63	30.52	0	0	0		
Ba-137m/Cs-137	0.662	Soil	0.08	1.60	7.94	31.77	0	0	0	0	0
		Concrete	0.08	2.30	5.59	22.35	0	0	0	0	0
		Wood	0.08	0.64	19.12	76.47	0	0	0	0	
		Steel	0.07	8.00	1.70	6.80	0	0	0	0	1
		Glass	0.08	2.40	5.41	21.64	0	0	0		
		Drywall	0.08	2.32	5.44	21.76	0	0	0		
I-129	0.040	Soil	0.51	1.60	1.22	4.87	0	0	0	1	1
		Concrete	0.54	2.30	0.81	3.22	0	0	0	1	1
		Wood	0.25	0.64	6.30	25.20	0	0	0	0	
		Steel	3.55	8.00	0.04	0.14	1	1	1	1	1
		Glass	0.59	2.40	0.71	2.83	0	0	1		
		Drywall	0.76	2.32	0.57	2.26	0	0	1		

Radionuclide	Energy (MeV)	Medium	Mass Attenuation Coefficient (cm^2/g)	Medium Density (g/cm^3)	Mean Free Path 1/μ (cm)	D 4/μ (cm)	1 cm depth	2 cm depth	3 cm depth	5 cm depth	15 cm depth
I-131	0.723	Soil	0.08	1.60	8.27	33.07	0	0	0	0	0
		Concrete	0.07	2.30	5.82	23.26	0	0	0	0	0
		Wood	0.08	0.64	19.89	79.58	0	0	0	0	
		Steel	0.07	8.00	1.78	7.10	0	0	0	0	1
		Glass	0.07	2.40	5.63	22.53	0	0	0		
		Drywall	0.08	2.32	5.66	22.66	0	0	0		
Pu-238	0.021	Soil	2.49	1.60	0.25	1.00	0	1	1	1	1
		Concrete	2.69	2.30	0.16	0.65	1	1	1	1	1
		Wood	0.63	0.64	2.48	9.90	0	0	0	0	
		Steel	21.91	8.00	0.01	0.02	1	1	1	1	1
		Glass	3.05	2.40	0.14	0.55	1	1	1		
		Drywall	4.16	2.32	0.10	0.41	1	1	1		
Pu-239	0.020	Soil	2.86	1.60	0.22	0.88	1	1	1	1	1
		Concrete	3.08	2.30	0.14	0.56	1	1	1	1	1
		Wood	0.70	0.64	2.23	8.91	0	0	0	0	
		Steel	25.12	8.00	0.00	0.02	1	1	1	1	1
		Glass	3.50	2.40	0.12	0.48	1	1	1		
		Drywall	4.78	2.32	0.09	0.36	1	1	1		
Pu-240	0.021	Soil	2.49	1.60	0.25	1.00	0	1	1	1	1
		Concrete	2.69	2.30	0.16	0.65	1	1	1	1	1
		Wood	0.63	0.64	2.48	9.90	0	0	0	0	
		Steel	21.91	8.00	0.01	0.02	1	1	1	1	1
		Glass	3.05	2.40	0.14	0.55	1	1	1		
		Drywall	4.16	2.32	0.10	0.41	1	1	1		
Ra-226	0.186	Soil	0.13	1.60	4.75	18.98	0	0	0	0	0
		Concrete	0.13	2.30	3.33	13.32	0	0	0	0	1

Radionuclide	Energy (MeV)	Medium	Mass Attenuation Coefficient (cm^2/g)	Medium Density (g/cm^3)	Mean Free Path 1/μ (cm)	D 4/μ (cm)	1 cm depth	2 cm depth	3 cm depth	5 cm depth	15 cm depth
		Wood	0.13	0.64	11.69	46.75	0	0	0	0	
		Steel	0.16	8.00	0.81	3.22	0	0	0	1	1
		Glass	0.13	2.40	3.21	12.84	0	0	0		
		Drywall	0.14	2.32	3.19	12.77	0	0	0		
Ra-228	0.016	Soil	5.37	1.60	0.12	0.47	1	1	1	1	1
		Concrete	5.80	2.30	0.07	0.30	1	1	1	1	1
		Wood	1.20	0.64	1.31	5.23	0	0	0	0	
		Steel	46.74	8.00	0.00	0.01	1	1	1	1	1
		Glass	6.62	2.40	0.06	0.25	1	1	1		
		Drywall	9.03	2.32	0.05	0.19	1	1	1		
Tc-99m	0.141	Soil	0.15	1.60	4.25	16.98	0	0	0	0	0
		Concrete	0.15	2.30	2.97	11.88	0	0	0	0	1
		Wood	0.15	0.64	10.70	42.81	0	0	0	0	
		Steel	0.21	8.00	0.59	2.37	0	0	1	1	1
		Glass	0.15	2.40	2.85	11.40	0	0	0		
		Drywall	0.15	2.32	2.80	11.21	0	0	0		
Th-228	0.216	Soil	0.12	1.60	5.02	20.10	0	0	0	0	0
		Concrete	0.12	2.30	3.53	14.12	0	0	0	0	1
		Wood	0.13	0.64	12.29	49.17	0	0	0	0	
		Steel	0.14	8.00	0.92	3.66	0	0	0	1	1
		Glass	0.12	2.40	3.41	13.63	0	0	0		
		Drywall	0.13	2.32	3.40	13.60	0	0	0		
Th-230	0.068	Soil	0.23	1.60	2.68	10.71	0	0	0	0	1
		Concrete	0.24	2.30	1.83	7.32	0	0	0	0	1
		Wood	0.18	0.64	8.47	33.89	0	0	0	0	
		Steel	0.86	8.00	0.15	0.58	1	1	1	1	1

Radionuclide	Energy (MeV)	Medium	Mass Attenuation Coefficient (cm^2/g)	Medium Density (g/cm^3)	Mean Free Path 1/μ (cm)	D 4/μ (cm)	1 cm depth	2 cm depth	3 cm depth	5 cm depth	15 cm depth
		Glass	0.25	2.40	1.69	6.77	0	0	0		
		Drywall	0.28	2.32	1.51	6.05	0	0	0		
Th-232	0.064	Soil	0.25	1.60	2.51	10.05	0	0	0	0	1
		Concrete	0.25	2.30	1.71	6.85	0	0	0	0	1
		Wood	0.19	0.64	8.28	33.10	0	0	0	0	
		Steel	1.00	8.00	0.12	0.50	1	1	1	1	1
		Glass	0.26	2.40	1.57	6.30	0	0	0		
		Drywall	0.31	2.32	1.39	5.55	0	0	0		
U-234	0.053	Soil	0.32	1.60	1.98	7.91	0	0	0	0	1
		Concrete	0.33	2.30	1.33	5.33	0	0	0	0	1
		Wood	0.21	0.64	7.59	30.37	0	0	0	0	
		Steel	1.64	8.00	0.08	0.31	1	1	1	1	1
		Glass	0.35	2.40	1.20	4.81	0	0	0		
		Drywall	0.42	2.32	1.02	4.07	0	0	0		
U-235	0.221	Soil	0.12	1.60	5.07	20.28	0	0	0	0	0
		Concrete	0.12	2.30	3.56	14.24	0	0	0	0	1
		Wood	0.13	0.64	12.39	49.56	0	0	0	0	
		Steel	0.13	8.00	0.93	3.73	0	0	0	1	1
		Glass	0.12	2.40	3.44	13.75	0	0	0		
		Drywall	0.13	2.32	3.43	13.73	0	0	0		
U-238/Pa-234m	1.001	Soil	0.06	1.60	9.65	38.58	0	0	0	0	0
		Concrete	0.06	2.30	6.79	27.14	0	0	0	0	0
		Wood	0.07	0.64	23.20	92.79	0	0	0	0	
		Steel	0.06	8.00	2.09	8.34	0	0	0	0	1
		Glass	0.06	2.40	6.57	26.29	0	0	0		
		Drywall	0.07	2.32	6.61	26.45	0	0	0		

Table A.3. Densities and mass attenuation coefficients and infinite thickness depths for six media for discrete gamma-ray emission energies.

Energy (MeV)	Medium	Mass Attenuation Coefficient (cm^2/g)	Medium Density (g/cm^3)	Mean Free Path 1/μ (cm)	D 4/μ (cm)	1 cm depth	2 cm depth	3 cm depth	5 cm depth	15 cm depth
0.02	Soil	2.856	1.60	0.22	0.88	1	1	1	1	1
	Concrete	3.079	2.30	0.14	0.56	1	1	1	1	1
	Wood	0.701	0.64	2.23	8.91	0	0	0	0	
	Steel	25.120	8.00	0.00	0.02	1	1	1	1	1
	Glass	3.499	2.40	0.12	0.48	1	1	1		
	Drywall	4.781	2.32	0.09	0.36	1	1	1		
0.03	Soil	0.977	1.60	0.64	2.56	0	0	1	1	1
	Concrete	1.042	2.30	0.42	1.67	0	1	1	1	1
	Wood	0.339	0.64	4.61	18.44	0	0	0	0	
	Steel	7.996	8.00	0.02	0.06	1	1	1	1	1
	Glass	1.164	2.40	0.36	1.43	0	1	1		
	Drywall	1.562	2.32	0.28	1.10	0	1	1		
0.04	Soil	0.513	1.60	1.22	4.87	0	0	0	1	1
	Concrete	0.539	2.30	0.81	3.22	0	0	0	1	1
	Wood	0.248	0.64	6.30	25.20	0	0	0	0	
	Steel	3.550	8.00	0.04	0.14	1	1	1	1	1
	Glass	0.589	2.40	0.71	2.83	0	0	1		
	Drywall	0.762	2.32	0.57	2.26	0	0	1		
0.05	Soil	0.345	1.60	1.81	7.25	0	0	0	0	1
	Concrete	0.358	2.30	1.22	4.86	0	0	0	1	1
	Wood	0.212	0.64	7.36	29.43	0	0	0	0	
	Steel	1.917	8.00	0.07	0.26	1	1	1	1	1
	Glass	0.382	2.40	1.09	4.36	0	0	0		

Energy (MeV)	Medium	Mass Attenuation Coefficient (cm^2/g)	Medium Density (g/cm^3)	Mean Free Path 1/μ (cm)	D 4/μ (cm)	1 cm depth	2 cm depth	3 cm depth	5 cm depth	15 cm depth
	Drywall	0.473	2.32	0.91	3.65	0	0	0		
0.06	Soil	0.268	1.60	2.33	9.32	0	0	0	0	1
	Concrete	0.275	2.30	1.58	6.33	0	0	0	0	1
	Wood	0.194	0.64	8.05	32.22	0	0	0	0	
	Steel	1.181	8.00	0.11	0.42	1	1	1	1	1
	Glass	0.288	2.40	1.45	5.79	0	0	0		
	Drywall	0.343	2.32	1.26	5.03	0	0	0		
0.07	Soil	0.227	1.60	2.75	11.01	0	0	0	0	1
	Concrete	0.230	2.30	1.89	7.55	0	0	0	0	1
	Wood	0.182	0.64	8.57	34.27	0	0	0	0	
	Steel	0.801	8.00	0.16	0.62	1	1	1	1	1
	Glass	0.238	2.40	1.75	6.99	0	0	0		
	Drywall	0.274	2.32	1.57	6.29	0	0	0		
0.08	Soil	0.202	1.60	3.09	12.37	0	0	0	0	1
	Concrete	0.204	2.30	2.13	8.53	0	0	0	0	1
	Wood	0.174	0.64	8.97	35.90	0	0	0	0	
	Steel	0.585	8.00	0.21	0.85	1	1	1	1	1
	Glass	0.209	2.40	2.00	7.99	0	0	0		
	Drywall	0.234	2.32	1.84	7.36	0	0	0		
0.1	Soil	0.174	1.60	3.59	14.36	0	0	0	0	1
	Concrete	0.174	2.30	2.50	9.98	0	0	0	0	1
	Wood	0.162	0.64	9.63	38.53	0	0	0	0	
	Steel	0.367	8.00	0.34	1.36	0	1	1	1	1
	Glass	0.176	2.40	2.37	9.47	0	0	0		
	Drywall	0.191	2.32	2.26	9.03	0	0	0		

Energy (MeV)	Medium	Mass Attenuation Coefficient (cm^2/g)	Medium Density (g/cm^3)	Mean Free Path 1/μ (cm)	D 4/μ (cm)	1 cm depth	2 cm depth	3 cm depth	5 cm depth	15 cm depth
0.15	Soil	0.144	1.60	4.36	17.42	0	0	0	0	0
	Concrete	0.143	2.30	3.05	12.20	0	0	0	0	1
	Wood	0.143	0.64	10.90	43.61	0	0	0	0	
	Steel	0.195	8.00	0.64	2.57	0	0	1	1	1
	Glass	0.142	2.40	2.93	11.73	0	0	0		
	Drywall	0.149	2.32	2.89	11.56	0	0	0		
0.2	Soil	0.128	1.60	4.88	19.52	0	0	0	0	0
	Concrete	0.127	2.30	3.43	13.70	0	0	0	0	1
	Wood	0.131	0.64	11.97	47.89	0	0	0	0	
	Steel	0.145	8.00	0.86	3.44	0	0	0	1	1
	Glass	0.126	2.40	3.30	13.22	0	0	0		
	Drywall	0.131	2.32	3.29	13.17	0	0	0		
0.3	Soil	0.110	1.60	5.70	22.81	0	0	0	0	0
	Concrete	0.108	2.30	4.01	16.04	0	0	0	0	0
	Wood	0.113	0.64	13.83	55.31	0	0	0	0	
	Steel	0.110	8.00	1.14	4.56	0	0	0	1	1
	Glass	0.108	2.40	3.88	15.50	0	0	0		
	Drywall	0.111	2.32	3.89	15.55	0	0	0		
0.4	Soil	0.098	1.60	6.40	25.60	0	0	0	0	0
	Concrete	0.097	2.30	4.50	18.00	0	0	0	0	0
	Wood	0.101	0.64	15.44	61.76	0	0	0	0	
	Steel	0.094	8.00	1.33	5.32	0	0	0	0	1
	Glass	0.096	2.40	4.35	17.42	0	0	0		
	Drywall	0.099	2.32	4.37	17.50	0	0	0		
0.5	Soil	0.089	1.60	7.02	28.09	0	0	0	0	0

Energy (MeV)	Medium	Mass Attenuation Coefficient (cm^2/g)	Medium Density (g/cm^3)	Mean Free Path 1/μ (cm)	D 4/μ (cm)	1 cm depth	2 cm depth	3 cm depth	5 cm depth	15 cm depth
	Concrete	0.088	2.30	4.94	19.76	0	0	0	0	0
	Wood	0.092	0.64	16.92	67.69	0	0	0	0	
	Steel	0.084	8.00	1.49	5.94	0	0	0	0	1
	Glass	0.087	2.40	4.78	19.13	0	0	0		
	Drywall	0.090	2.32	4.81	19.23	0	0	0		
0.6	Soil	0.082	1.60	7.60	30.41	0	0	0	0	0
	Concrete	0.081	2.30	5.35	21.39	0	0	0	0	0
	Wood	0.085	0.64	18.30	73.22	0	0	0	0	
	Steel	0.077	8.00	1.62	6.49	0	0	0	0	1
	Glass	0.080	2.40	5.18	20.71	0	0	0		
	Drywall	0.083	2.32	5.21	20.82	0	0	0		
0.8	Soil	0.072	1.60	8.66	34.65	0	0	0	0	0
	Concrete	0.071	2.30	6.09	24.38	0	0	0	0	0
	Wood	0.075	0.64	20.84	83.38	0	0	0	0	
	Steel	0.067	8.00	1.86	7.46	0	0	0	0	1
	Glass	0.071	2.40	5.90	23.61	0	0	0		
	Drywall	0.073	2.32	5.94	23.75	0	0	0		
1	Soil	0.065	1.60	9.64	38.56	0	0	0	0	0
	Concrete	0.064	2.30	6.78	27.13	0	0	0	0	0
	Wood	0.067	0.64	23.19	92.74	0	0	0	0	
	Steel	0.060	8.00	2.08	8.34	0	0	0	0	1
	Glass	0.063	2.40	6.57	26.27	0	0	0		
	Drywall	0.065	2.32	6.61	26.44	0	0	0		
1.5	Soil	0.053	1.60	11.84	47.37	0	0	0	0	0
	Concrete	0.052	2.30	8.33	33.32	0	0	0	0	0

Energy (MeV)	Medium	Mass Attenuation Coefficient (cm^2/g)	Medium Density (g/cm^3)	Mean Free Path 1/μ (cm)	D 4/μ (cm)	1 cm depth	2 cm depth	3 cm depth	5 cm depth	15 cm depth
	Wood	0.055	0.64	28.49	113.95	0	0	0	0	
	Steel	0.049	8.00	2.56	10.23	0	0	0	0	1
	Glass	0.052	2.40	8.07	32.26	0	0	0		
	Drywall	0.053	2.32	8.12	32.46	0	0	0		
2	Soil	0.045	1.60	13.74	54.97	0	0	0	0	0
	Concrete	0.045	2.30	9.66	38.65	0	0	0	0	0
	Wood	0.047	0.64	33.19	132.75	0	0	0	0	
	Steel	0.043	8.00	2.93	11.72	0	0	0	0	1
	Glass	0.045	2.40	9.35	37.40	0	0	0		
	Drywall	0.046	2.32	9.41	37.62	0	0	0		
3	Soil	0.037	1.60	16.92	67.68	0	0	0	0	0
	Concrete	0.037	2.30	11.88	47.50	0	0	0	0	0
	Wood	0.038	0.64	41.35	165.39	0	0	0	0	
	Steel	0.036	8.00	3.45	13.81	0	0	0	0	1
	Glass	0.036	2.40	11.47	45.88	0	0	0		
	Drywall	0.037	2.32	11.53	46.11	0	0	0		

Table A.4. Densities and mass attenuation coefficients and infinite (4) mean free path depths for discrete gamma-ray emission energies to define contamination plane radius.

Energy (MeV)	Mass Attenuation Coefficient μ/ρ (cm^2/g)	Linear Attenuation Coefficient μ (cm^{-1}) -	Mean Free Path $1/\mu$ (cm)	Plane Radius $4/\mu$ (cm)
0.01	5.120	6.62E-03	151.05	604.22
0.02	0.778	1.01E-03	994.21	3976.84
0.03	0.354	4.57E-04	2185.97	8743.87
0.04	0.249	3.21E-04	3112.25	12449.02
0.05	0.208	2.69E-04	3718.25	14872.98
0.06	0.188	2.42E-04	4124.77	16499.10
0.07	0.177	2.29E-04	4389.09	17556.35
0.08	0.166	2.15E-04	4653.40	18613.60
0.1	0.154	1.99E-04	5018.79	20075.15
0.15	0.136	1.75E-04	5703.50	22814.02
0.2	0.123	1.59E-04	6272.47	25089.87
0.3	0.107	1.38E-04	7248.31	28993.26
0.4	0.095	1.23E-04	8099.23	32396.91
0.5	0.087	1.13E-04	8877.36	35509.42
0.6	0.081	1.04E-04	9601.43	38405.72
0.8	0.071	9.15E-05	10932.93	43731.71
1	0.064	8.22E-05	12164.13	48656.51
1.5	0.052	6.69E-05	14944.83	59779.34
2	0.044	5.75E-05	17391.39	69565.57
3	0.036	4.63E-05	21597.19	86388.74

APPENDIX B. Supplemental Figures

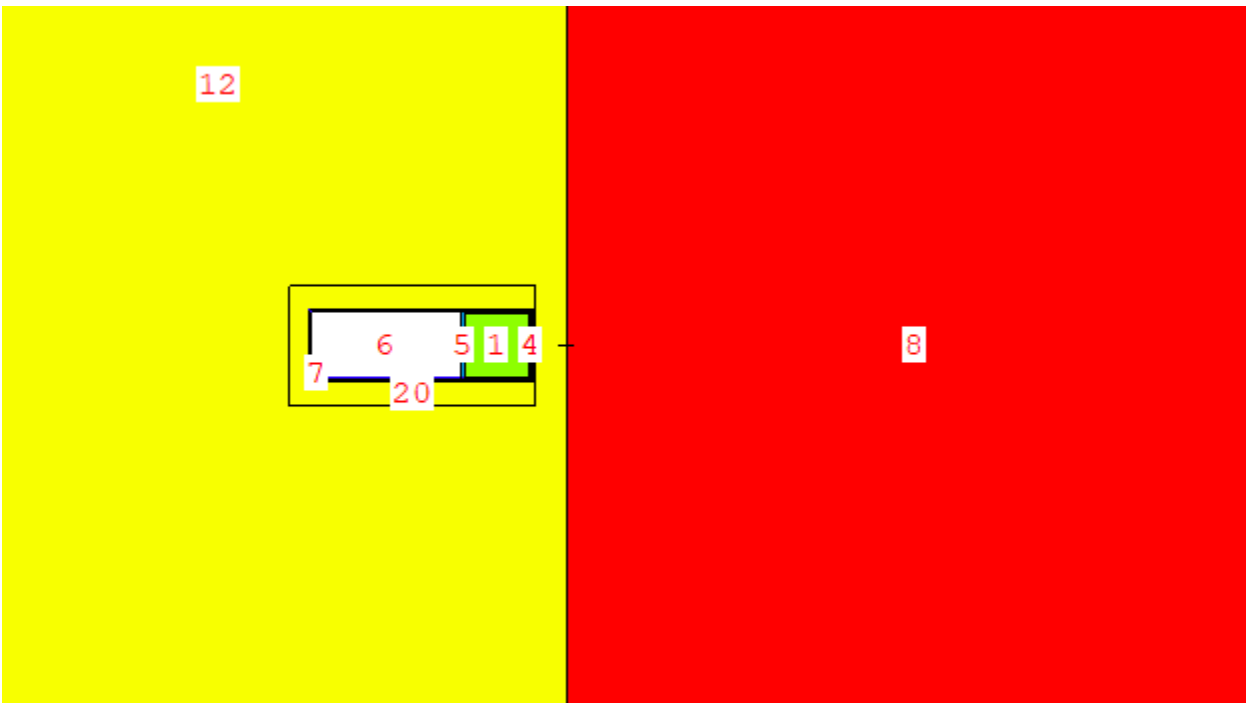

Figure B.1. MCNPX Visual Editor rendering of a 2x2-inch detector response problem geometry.

The NaI(Tl) detector crystal tally region is denoted by cell 1 in green. The detector is surrounded by air (yellow). The contaminated medium in this example is soil (red). The problem geometry is cylindrically-shaped; photons will travel from the medium in the *x*-direction to reach the detector (Schwarz et al., 2011).

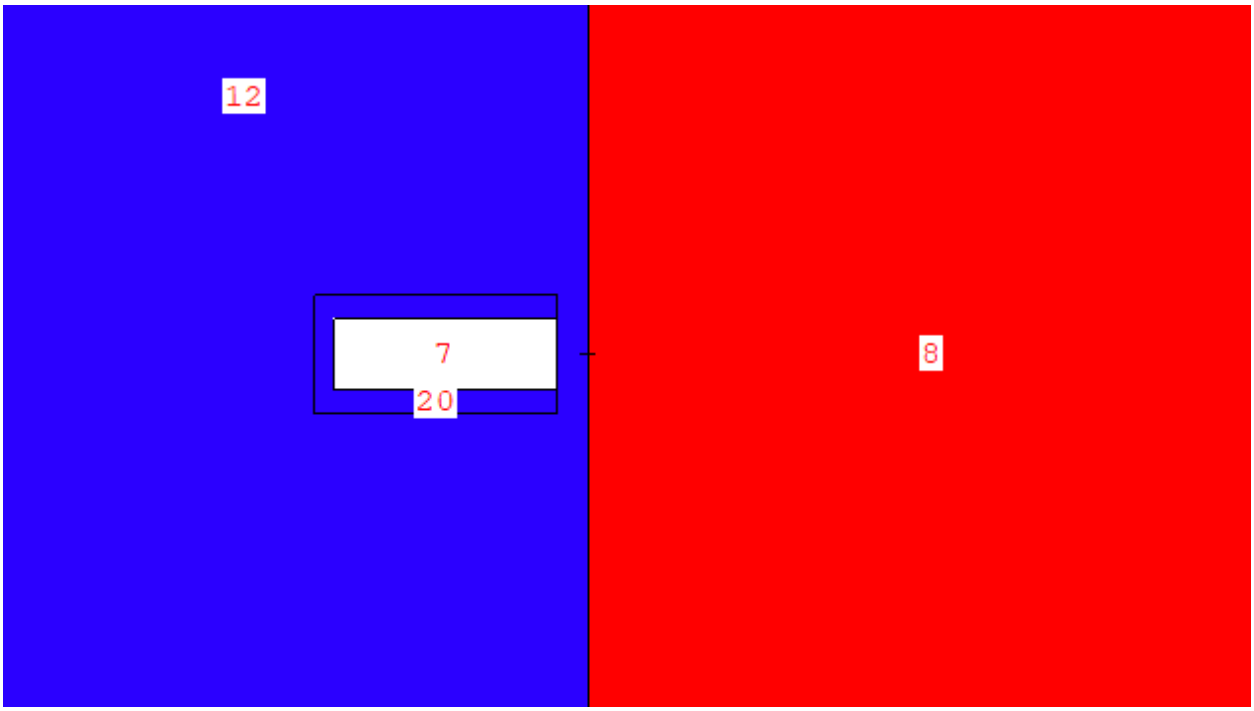

Figure B.2. MCNPX Visual Editor rendering of a 2x2-inch void detector response problem geometry.

The entire 2x2-inch configuration in Figure B1 is filled with a void (cell 7). The detector is surrounded by air (blue). The contaminated medium in this example is soil (red). The problem geometry is cylindrically-shaped; photons will travel from the medium in the *x*-direction to reach the detector. The void flux in the detector region is converted to a detector response value after interpolating over the appropriate response function (Schwarz et al., 2011).

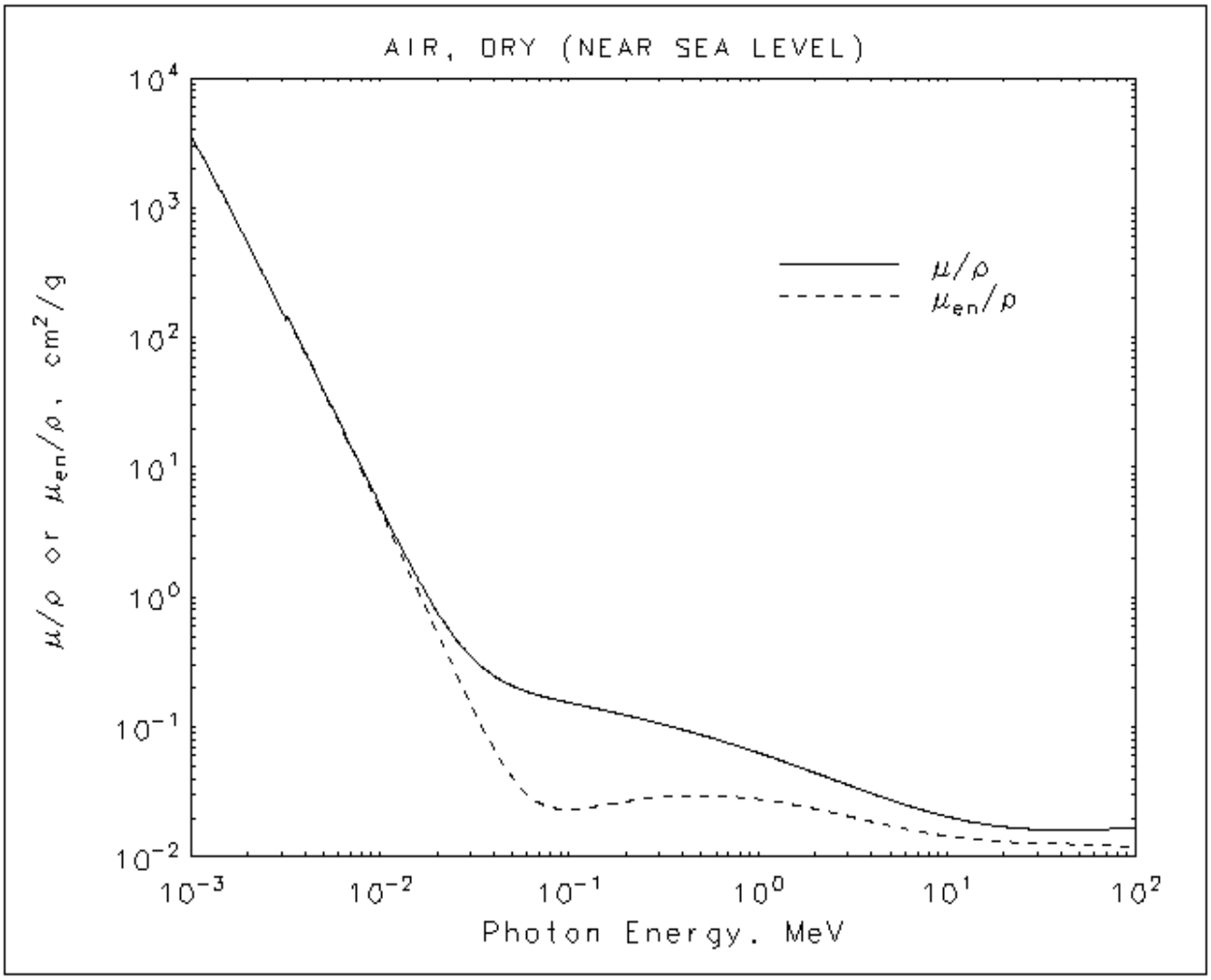

Figure B.3. Total mass attenuation coefficient and energy absorption mass coefficient as a function of photon energy in air (Berger et al,. 2010).

APPENDIX C. List of Electronically Tabulated Data

All electronic tabulated data are available via the ORNL Dropbox.
The Dropbox is structured according to the following schema:

```
Medium (6)
        |_ Contamination Depth (variable according to medium, per Table 1)
                |_ GroundPlane
                |_ 1 cm
                |_ 2 cm
                |_ 5 cm
                |_ 15 cm
                        |_Monoenergetic Energies (19 per Table 2)
                        |_Radionuclides (21 per Tables A2 and A3)
                                |_Detector Model (4 per SOW)
                                        |_ 5 distances (0.5, 1, 2.54, 10, 30 cm)
```

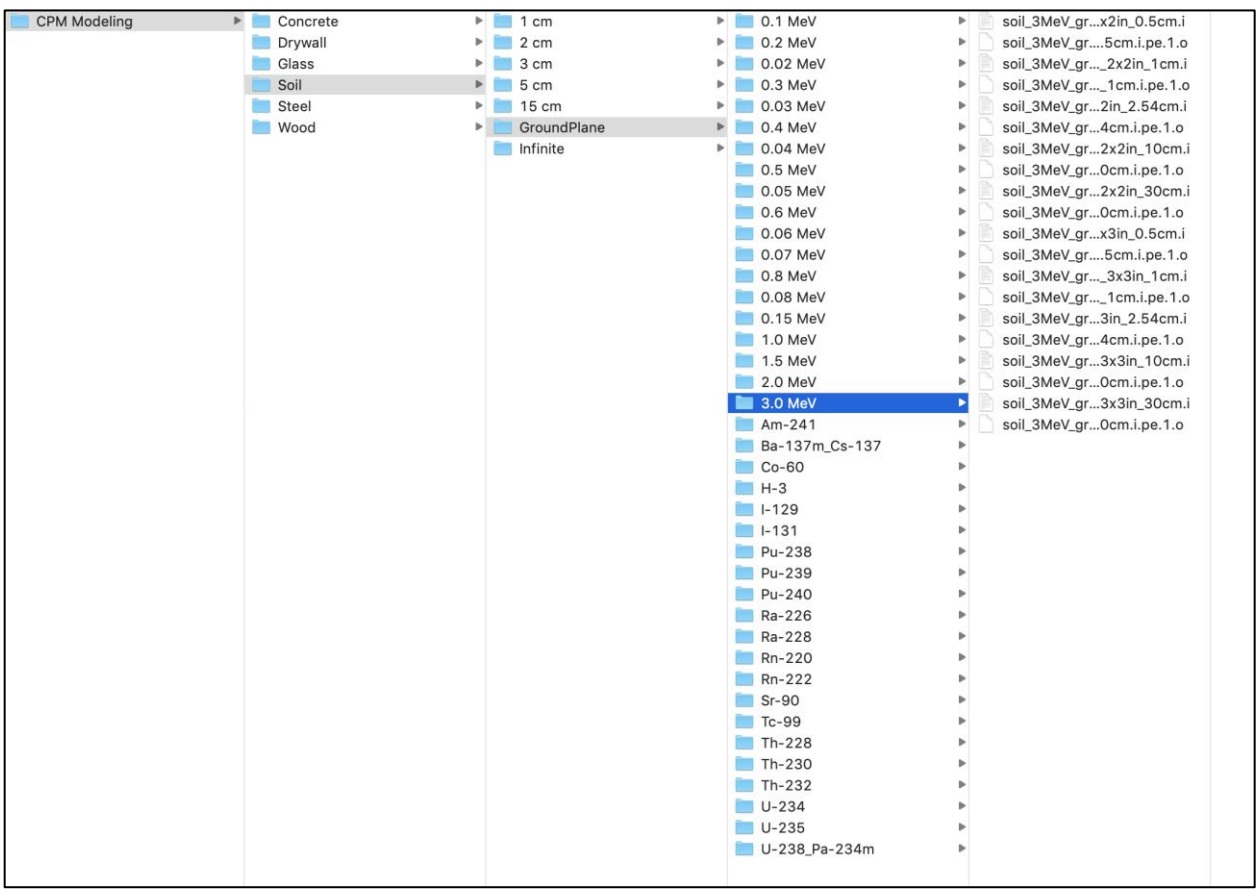

Figure C.1. Electronic data format for CPM model (input/output) and response function data.

Surface CPM MCNP Input and Output
Filename: << *medium_energy or nuclide_media_depth_detector_distance.extension* >>

.i = MCNP input deck
.o = MCNP output

Example:

The file naming for 3 MeV photons on the surface (groundplane) for the 2x2 NaI(Tl) detector located 1 cm from the surface of a soil medium is:

soil_3MeV_groundplane_2x2in_1cm.i
soil_3MeV_groundplane_2x2in_1cm.o

Note: Continue-run MCNP outputs in the shared dropbox may have a slightly modified file extension due to runtpe file iteration while multithreading (i.e. ".i.pe.1.o").

Volume CPM Shift Input and Output

Filename: << *medium_energy or nuclide_media_depth_detector_distance.extension* >>

.omn = SHIFT omnibus input deck
.csv = SHIFT output spreadsheet

The energy-binned and total results (i.e. average cell flux) will be extracted from SHIFT with associated relative errors for each omnibus input deck into a .csv file.

Example:

The file naming for 3 MeV photons on the surface (groundplane) for the 2x2 NaI(Tl) detector located 1 cm from the surface of a soil medium for the average cell flux tally defined as "F4 cell flux" within SHIFT is:

soil_3MeV_groundplane_2x2in_1cm.omn
soil_3MeV_groundplane_2x2in_1cm.F4_cell_flux.csv

Final Activity to CPM Conversion Factor Output

In addition to the provided I/O files from MCNP and SHIFT, TAMU will transmit the final area and volume activity to cpm conversion factors defined in §3.5 as a function of 1024 energy bins. The total output value will also be provided for convenience. The area conversion factors will have an associated relative error extracted from MCNP. The volume conversion factors will not have an associated relative error since error propagation of SHIFT results is not currently supported by TAMU post-processing methods. However, it should be noted that all SHIFT average cell flux values will have an associated relative error of less than 5%; therefore, it may be assumed that all

interpolated detector response values will have reached proper convergence (in MCNP, average cell flux relative errors are consistently higher than corresponding pulse height relative errors).